博士論文

Screening effects on excitons in air-suspended carbon nanotubes

（架橋カーボンナノチューブにおける励起子の遮蔽効果に関する研究）

宇田 拓史

THE UNIVERSITY OF TOKYO

Screening effects on excitons in air-suspended carbon nanotubes

A thesis submitted in partial satisfaction
of the requirements for the degree of

Doctor of Philosophy

in

Engineering

by

Takushi Uda

37-157097

Thesis Advisors
Professor Seigo Tarucha
Associate Professor Yuichiro K. Kato

March 2018

Screening effects on excitons in air-suspended carbon nanotubes

by

Takushi Uda

Acknowledgments

I would like to first thank Prof. Kato, not just for his scientific advice and guidance, but also for teaching me how to write manuscript and make a presentation. The 5 year I spent with him was the most fruitful time in my life.

I also appreciate all the current members in Kato group. Great thanks to A. Ishii for many suggestions on my experiments and beneficial discussion. H. Machiya gave me nice information on cavity quantum electrodynamics and information equipment. G. Widianta helped to stabilize our room temperature and taught a lot about his country.

Of the pas group members, I would like to express my special gratitude to N. Higashide. Various discussions beyond experiments were very fun, and without such gratiful time, it would be difficult to overcome many difficulties. I also thank Dr. Yoshida for giving me a lot advice on experiments and English presentation. I also spent valuable time at Kato group with R. Miura, M. Jiang, X. Liu, S. Lee, K. Fujisawa, I. Kimura, A. Sasabe, Y. Ueda, K. Takahashi, and T. Shimada. I learned a lot from them. Many international internship students joined our group, and we had a lot of fun time. In particular, A. Subramanian helped to investigate the environmental effects. The time spent working with him was a wonderful moment. A. Unterkreuter, K. Ozvoldik, S. Stuij, J. Jung, E. Rofers, A. Popert, S. Feng, also give me a lot of opportunity to learn and improve my in English communication skills.

Great thanks to Nakamura-san, Hirosawa-san, Sawamura-san, Dr. Kubota, Dr. Mizushima, Prof. Mita, and technical assistants in Takeda clean room for managing a lot of instruments. I thank Prof. Shimoyama, Dr. Kan and Dr. Isozaki for the use of e-beam evaporator, and also thank Dr. Inoue, Prof. Chiashi, and Prof. Maruyama for use of an electron microscope and helpful discussion. I appreciate Prof. Tarucha for accepting me to his group, and Prof. Arakawa for advising me as a mentor of ALPS program. I had many precious experiences at Surface and Interface Science Laboratory, and thank Dr. Imada, and Kimura, and all the other group members. I thank JSPS and ALSP for supporting my research activities.

Finally, I would like to thank my parents for always being supportive of me.

Abstract

Screening effects on excitons in air-suspended carbon nanotubes

by

Takushi Uda

The unique optical properties of single-walled carbon nanotubes make them a promising material for nanoscale photonic and optoelectronic devices. The optical transitions are dominated by tightly bound excitons even at room temperature, as the limited screening in the one-dimensional systems results in an enhancement of the Coulomb interactions.

Here we show that the screening effects on excitons are particularly limited in air-suspended nanotubes. We examine electric field effects on various excitonic states by simultaneously measuring both photocurrent and photoluminescence. As the applied field increases, we observe an emergence of new absorption peaks in the excitation spectra. From the diameter dependence of the energy separation between the new peaks and the ground state of E_{11} excitons, we attribute the peaks to the dark excited states which became optically active due to the applied field. Field-induced exciton dissociation can explain the photocurrent threshold field, and the edge of the E_{11} continuum states has been identified by extrapolating to zero threshold. By taking the energy difference between the E_{11} continuum edge and ground state of E_{11} excitons, we have obtained exceptionally large exciton binding energies of 620 meV for air-suspended nanotubes.

We also show that the large screening effects on excitons give rise to all-optical memory functionality in individual carbon nanotubes. Excitation power and energy resolved photoluminescence microscopy reveals that resonance shifts induced by molecular adsorption and desorption leads to optical bistability. We demonstrate reversible and reproducible optical memory operation, and further perform time-resolved measurements to determine the rewriting speed.

Our results underscore the impact of molecular-scale screening effects on optical properties of nanomaterials, offering new design strategies for photonic devices that are a few orders of magnitude smaller than the optical diffraction limit.

Contents

Chapter 1

Introduction

In this chapter, we first introduce the physical properties of carbon nanotubes and show how the tubes are appealing for fundamental studies on excitonic physics as well as photonics and optoelectronic applications. We then explain the importance of screening effects on the optical properties of carbon nanotubes, with reviewing previous works on exciton binding energies and the environmental effects on the excitonic states. Finally, we present our research objective.

1.1 Single-walled carbon nanotubes

1.1.1 Atomic structure

A single-walled carbon nanotube has a structure of a rolled-up graphene sheet (Figure 1.1) [1]. The diameters are around 1 nm while the length can be more than 1 μm, and therefore carbon nanotubes can be viewed as quasi-one dimensional systems. The nanoscale diameters enhance the many-body effects [2] and quantize the electronic states [3], while their micron scale length allows integration into electronic [4–9] and photonic devices [10–13]. The chiral vector $\boldsymbol{L}$, which refer to how the tube is rolled-up from graphene, are expressed by using two lattice vectors $\boldsymbol{a}_1$ and $\boldsymbol{a}_2$ as,

$$\boldsymbol{L} = n\boldsymbol{a}_1 + m\boldsymbol{a}_2 \equiv (n, m), \tag{1.1}$$

where n and m are integers, and the pair of the integers (n, m) is called chirality. Unlike the other nanomaterials, the structures of carbon nanotubes can be

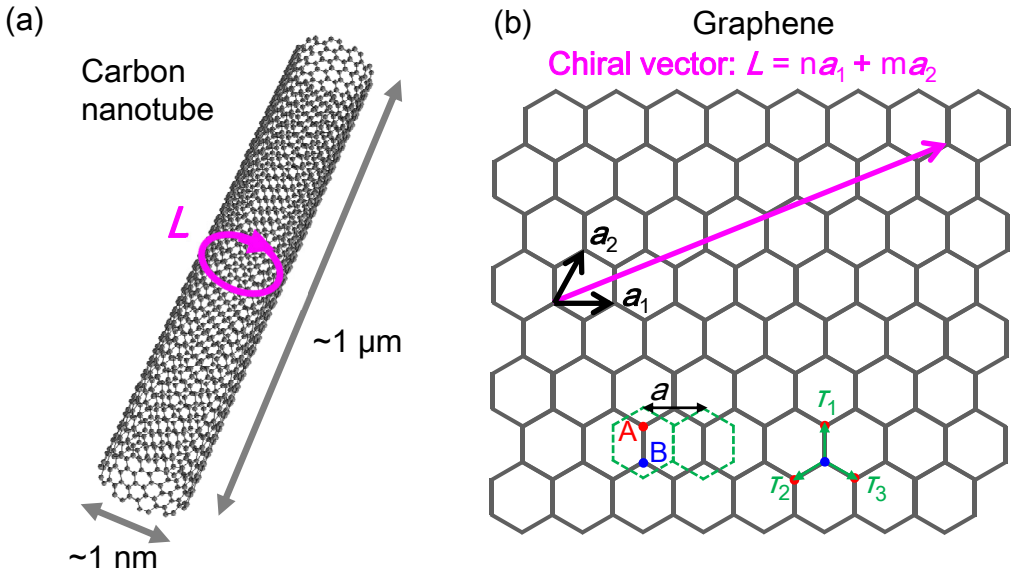

Figure 1.1: (a) Structure of a single-walled carbon nanotube. (b) The chiral vector drawn on a single layer of graphene. a1 and a2 are the lattice vectors of the graphene hanycomb structure.

uniquely determined from this chirality.

1.1.2 Electronic structure

Dispersion relations of electrons in carbon nanotubes can be obtained by introducing the circumferential periodic boundary condition into the graphene band structures. Here we give a brief introduction to the band structure of nanotubes based on the description in Ref. [14].

Graphene

As shown in Figure 1.1, a single layer of graphene consists of carbon atoms arranged in a hexagonal lattice. There are two carbon atoms denoted by A and B in the unit cell of a graphene, and we represent their position vector by $\mathbf{R}_{\mathrm{A}}$ and $\mathbf{R}_{\mathrm{B}}$, respectively. The unit cells are separated with period a. There are three nearest neighbor atoms at a distance of $a/\sqrt{3}$, which we represent the displacement vectors by τ_l $(l = 1, 2, 3)$. In a tight-binding model, the wave

function of electrons in such a structure can be expressed as

$$\Psi(\mathbf{r}) = \sum_{\mathbf{R}_A} C_{\mathrm{A}} e^{i\mathbf{k}\cdot\mathbf{R}_A} \phi(\mathbf{r} - \mathbf{R}_A) + \sum_{\mathbf{R}_B} C_{\mathrm{B}} e^{i\mathbf{k}\cdot\mathbf{R}_B} \phi(\mathbf{r} - \mathbf{R}_B), \tag{1.2}$$

where we let $\phi(\mathbf{r})$ be p_{z} orbital wave function of carbon atom located at the origin. If we neglect the overlap integral between A and B sites, the electron energy ε should follow

$$\varepsilon C_{\mathrm{A}} e^{i\mathbf{k}\cdot\mathbf{R}_A} = -\gamma_0 \sum_{l=1}^{3} C_{\mathrm{B}} e^{i\mathbf{k}\cdot(\mathbf{R}_A - \tau_l)} \tag{1.3}$$

$$\varepsilon C_{\mathrm{B}} e^{i\mathbf{k}\cdot\mathbf{R}_B} = -\gamma_0 \sum_{l=1}^{3} C_{\mathrm{A}} e^{i\mathbf{k}\cdot(\mathbf{R}_B - \tau_l)}, \tag{1.4}$$

where we let γ_0 be the transfer integral between nearest-neighbor carbon atoms. By solving these simultaneous equations, we obtain

$$\varepsilon_{\pm}(\boldsymbol{k}) = \pm\gamma_0 \sqrt{1 + 4\cos\frac{ak_x}{2}\cos\frac{\sqrt{3}ak_y}{2} + 4\cos^2\frac{ak_x}{2}}. \tag{1.5}$$

At $K = (2\pi/3a, 2\pi/\sqrt{3}a)$ and $K' = (4\pi/3a, 0)$, the energies $\varepsilon(K)$ and $\varepsilon(K')$ are 0, showing that the conduction and valence bands touch at these points. Near the K and K' points ($|\delta\boldsymbol{k}|a << 1$), the energy dispersion is given by

$$\varepsilon_{\pm}(\boldsymbol{K} + \delta\boldsymbol{k}) \simeq \pm\gamma|\delta\boldsymbol{k}|, \tag{1.6}$$

where $\gamma \equiv \sqrt{3}a\gamma_0/2$. This linear band structure at around the Fermi level is well known as the Dirac cone.

Carbon nanotubes

Due to the cylindrical structure of carbon nanotubes, periodic boundary condition along the circumference direction is imposed on the wavenumber, which is expressed as

$$\exp(i\boldsymbol{k}\cdot\boldsymbol{L}) = 1. \tag{1.7}$$

In Figure 1.2, we show lines satisfying the boundary condition on the Brillouin zone of graphene. The lines are discrete with a period of $2\pi/L$ in the

circumference direction. To understand the band structure near the K point, we have

$$\exp(i\boldsymbol{K}\cdot\boldsymbol{L}) = \exp[\frac{2\pi i}{3}(n+2m)] = \exp(\frac{2\pi i}{3}\nu), \tag{1.8}$$

where ν is determined by

$$n - m \equiv \nu \pmod 3. \tag{1.9}$$

It is clear from this equation that the lines cross the K (and also K') point when $\nu = 0$. In this case there is no gap between the conduction and valence bands, and therefore these types of tubes are metallic. The equation also shows that the line always passes through a point displaced by $-2\pi\nu/3L$ in the circumference direction from the K point. The distances of the nth lines from the K point are, therefore,

$$\kappa_\nu = \frac{2\pi}{L}(n - \frac{\nu}{3}), \tag{1.10}$$

and the energies are

$$\varepsilon_\pm(n,k) \simeq \pm\gamma\sqrt{\kappa_\nu^2(n) + k^2}, \tag{1.11}$$

where k is the wavenumber perpendicular to κ_ν. There are band gaps when $\nu \neq 0$ and these types of tubes are semiconductors. As the bottom of the conduction band and the maximum of the valence band are at the same k-vector, semiconducting nanotubes are direct band gap materials, and therefore the tubes can absorb and emit photons. Since the band gap energies vary with their circumferences (or diameter), semiconducting nanotubes emit photons in broad wavelength range from near-infrared to telecommunication wavelengths [15–19].

1.2 Excitons in carbon nanotubes

1.2.1 Density of states and selection rules

One dimensional nature of carbon nanotubes makes their density of states (DOS) to have Van Hove singularities. The peaks in the conduction bands and valence

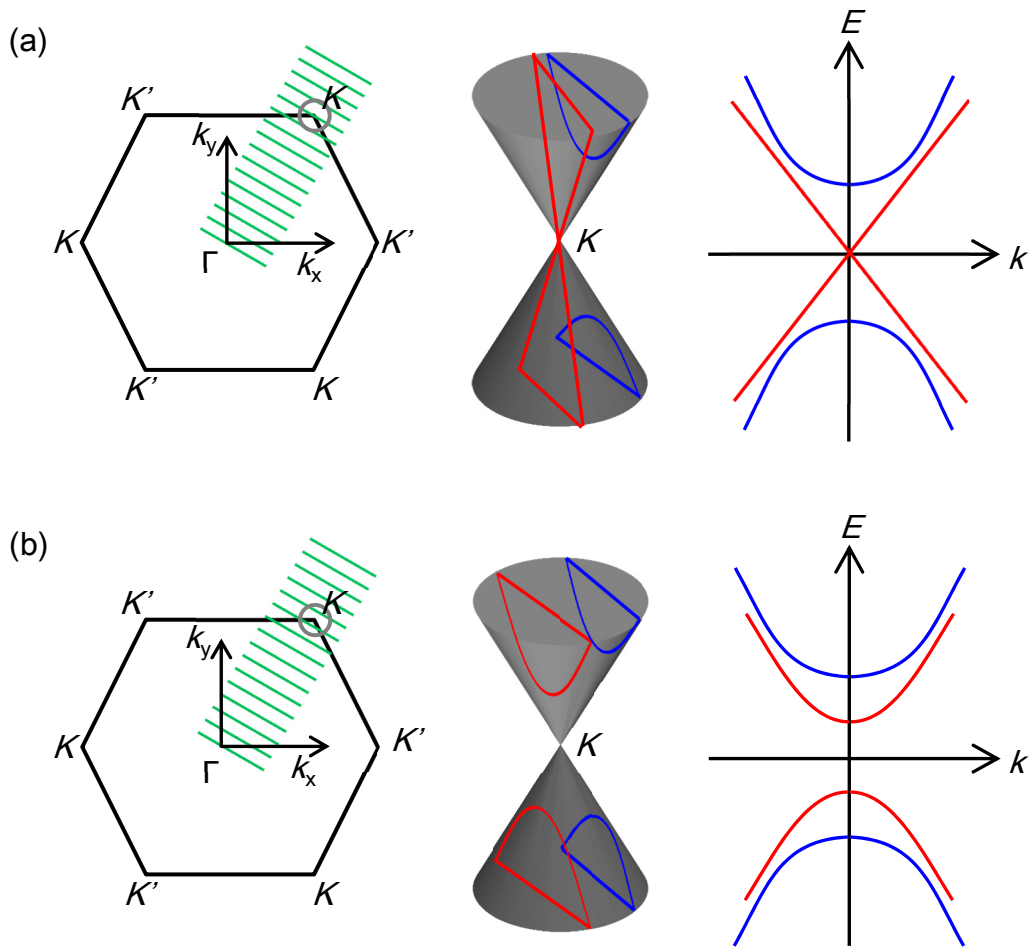

Figure 1.2: Allowed k lines of (a) a metalic nanotube and (b) a semiconducting nanotube in the Birillouin zone of graphene, and the corresponding dispersion relations of the electrons.

bands are labeled as $c_1, c_2, \ldots$ and $v_1, v_2, \ldots$ respectively (Figure 1.3a). Most of optical transitions occur between these singularities.

Conservation of the total angular momentum in the photon absorption process imposes selection rules on the band to band transitions. For the parallel polarization excitation, the angular quantum number of the electrons in the bands should not be changed, and therefore only $c_i v_i$ (E_{ii}) transitions are allowed. Conversely, the perpendicular excitation requires changes of the angular quantum number of the electrons by ± 1, and therefore only the transitions between the adjacent bands (such as $c_1 v_2$, $c_2 v_1$, $c_1 v_3$...) are allowed.

The perpendicular optical absorption is, however, suppressed because of depolarization effects [20, 21]. In the perpendicular excitation, charges are induced

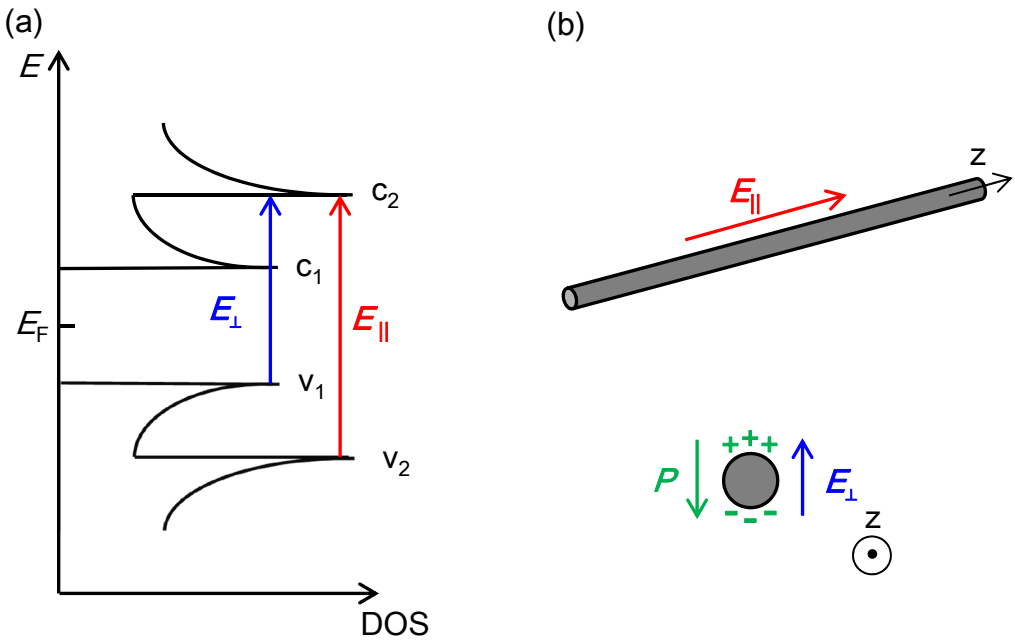

Figure 1.3: (a) Density states of a semiconducting carbon nanotubes and a schematic of the selection rules for the electronic transitions by incident light polarized parallel ($E_{\parallel}$) and perpendicular ($E_{\perp}$) to the tube axis. (b) Shcematics of induced carriers under external fields. P indicates induced polarization.

on the cylinder walls. These carriers form polarization vector against the external fields, resulting in a reduction of the total electric fields (Figure 1.3(b)). Such an effect is not appearing in the case of parallel excitation, and therefore most of the photon absorption is dominated by E_{ii} transitions.

1.2.2 Excitonic optical transitions

The strong Coulomb interactions in the one-dimensional systems cause modifications on the optical transition energies obtained from the single particle picture. As one can be seen from the fact that the exciton binding energy becomes infinitely large in ideal one dimensional system, the excitonic effect on the optical transition energies of nanotubes are quite important [2, 22]. The exciton wave function for an electron and a hole in the K valleys follows the Bethe-Salpeter

equation

$$\begin{aligned}\varepsilon_n\psi_n(k) = (2\gamma\sqrt{\kappa_\nu^2(n)+k^2} + \Delta\Sigma_{n,k})\psi_n(k) \\ - \sum_{m,q} V_{(+,n,k;+,m,k+q)(-,m,k+q;-,n,k)}\psi_m(k+q),\end{aligned} \tag{1.12}$$

where $V_{(\alpha_\mathrm{f};\alpha_\mathrm{i})(\beta_\mathrm{f};\beta_\mathrm{i})}$ indicates the interaction kernel between the carriers initially at the state of α_i and β_i, and finally at the states of α_f and β_f. + and - denote the conduction and valence band, respectively. $\Delta\Sigma_{n,k}$ indicate the difference of the self-energy between the conduction and valence band which is expressed in the conventional screened Hartree-Fock approximation as

$$\Delta\Sigma_{n,k} = \sum_{m,q} V_{(-,n,k;-,m,k+q)(-,m,k+q;-,n,k)} - V_{(+,n,k;-,m,k+q)(-,m,k+q;+,n,k)}, \tag{1.13}$$

at zero temperature. According to the Bethe-Salpeter equation, the strong electron-electron interaction renormalizes the band gap to a higher energy side, while strong electron-hole attractive interaction results in shifting the energy to the lower side (Figure 1.4) [2]. In a manner similar to the Rydberg states in atomic hydrogen, the excitons have a series of excited states. Because of the large binding energies of excitons, the excited excitonic states are discrete enough to be spectroscopically identified even at room temperature [23–26]. There are also continuum states, where electrons and holes are free. The edge of the continuum states match the electrical band gap. Note that the self-energy contribution is larger than the ground-exciton binding energy and therefore the optical transition energy is shifted to a higher side from the single particle picture [2]. Optical transition intensities to the excited states and continuum states are weak, as the transition intensities are concentrated in the lowest exciton states. Most of optical studies have investigated the ground exciton states which belong to the E_{ii} bands and the energies are commonly used for chirality assignment [16, 17], while the detailed photoluminescence excitation spectroscopy [23–25, 27] as well as absorption spectroscopy [26] show the existence of the excited excitonic states.

1.2.3 Fine structures of excitons

Due to the two equivalent valleys (K and K') in the momentum space in carbon nanotubes, there are four possible electron-hole combinations (KK, KK', $K'K$,

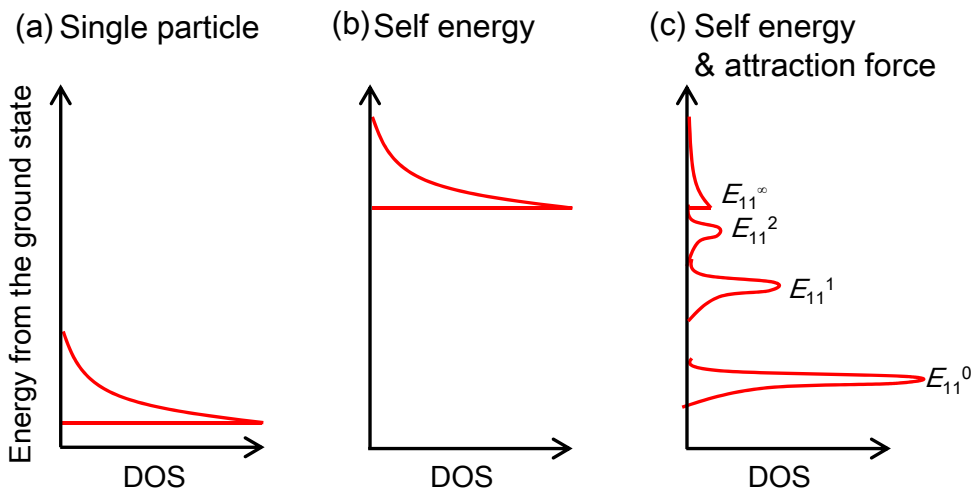

Figure 1.4: Schematic of the optical density of states obtained with (a) single particle picture, (b) Coulomb self-energy, and (c) Coulomb self-energy and excitonic interactions. Note that the band lift due to the self-energy contains both conduction- and valence-band shifts.

$K'K'$) to form excitons (Figure 1.5) [20, 28, 29]. In addition, these four possible states are further classified into four singlet and twelve triplet exciton states due to the spin degree of freedom. The triplet states are optically forbidden because the spin-orbit coupling is weak in carbon nanotubes. KK' and $K'K$ excitons (K-momentum excitons) are also optically forbidden, since a large momentum is required to the transitions. Remaining two degenerate direct singlet pairs create bonding and anti-bonding combinations, resulting in a formation of excitons with odd and even parity wave functions upon axial parity operation. The states with odd parity are optically accessible, while the states with even parity are not. Among the sixteen possible electron-hole combinations, only one exciton state can be excited by optical means.

The even parity states of excited excitonic states have been investigated via two-photon excitation spectroscopy [23, 24]. Temperature dependence measurements on the PL intensity shows that the parity forbidden state of the ground excitons exists few meV bellow the emission states [30, 31]. Emission form such an underlying dark state has been directly observed by breaking the symmetry via magnetic fields [30, 32–34] as well as impurity induced electric fields [35].

The triplet state has been observed by introducing laser induced defects, which increase the spin-orbit coupling and lead spin-flip process [36,37]. EuS coating [38]

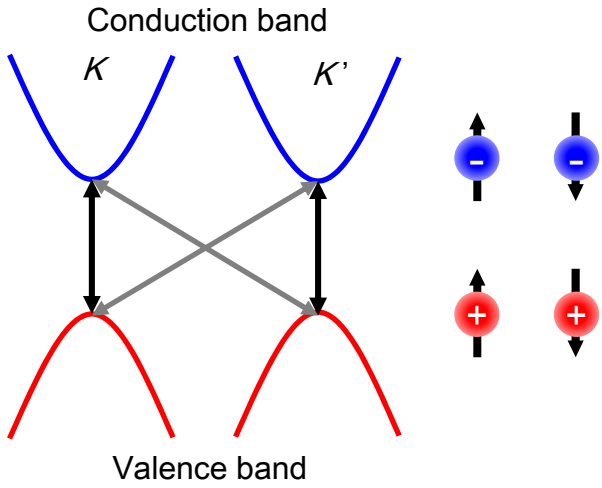

Figure 1.5: The four possible electron-hole pair in K and K' valleys, and electrons and holes with up and down spin.

as well as hydrogen adsorption [39] are also used to brighten the triplet states. In addition, the dynamics of the triplet states have been investigated by pump-probe and spin-sensitive PL studies [40].

1.3 Screening effects on excitons

1.3.1 Environmental effects on excitons

Despite the fact that structures of carbon nanotubes are uniquely determined from chirality, their optical transition energies differ if the environmental dielectric constants are changed. As most of the electric fields of carriers go through the outside of the cylindrical wall (Figure 1.6), the Coulomb interactions are easily screened by the surrounding medium, and it results in considerable modification on the optical properties. Such screening effects cause the difference of the emission energies from various type of tubes such as, bundling [41], surfactant suspension [17], DNA wrapping [42], and air-suspended nanotubes [18, 43].

Since the screening weakens both the self-energy and the binding energy, and also since the shifts are in opposite directions, significantly larger modification on the exciton binding and electrical band-gap energies should be taking place compared with emission energy. In particular, exciton binding and electrical

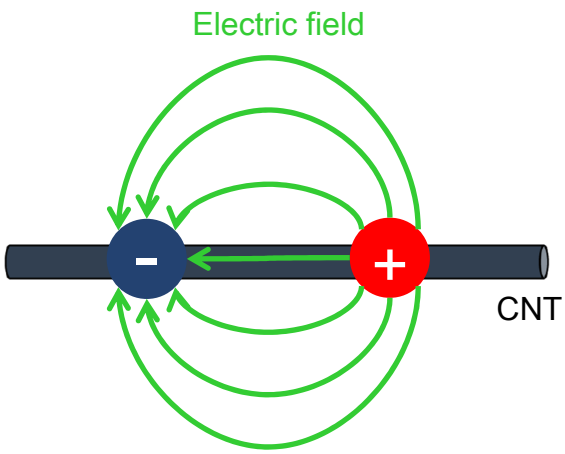

Figure 1.6: A schematic of the electric-field lines of an electron-hole pair in a carbon nanotube.

band-gap energies in air-suspended carbon nanotube should be significantly larger than those for micelle-wrapped tubes.

The exciton binding energies of the micelle-wrapped tubes have been investigated via two-photon excitation spectroscopy [23, 24], voltage-dependence measurements on Raman scattering intensity [44], and ultrafast transient absorption spectroscopy [45]. In the case of air-suspended carbon nanotubes, detailed PL excitation spectroscopy on excited excitonic states have been performed, and the evidence of the larger Coulomb interactions are obtained [25], but reliable determination of the exciton binding energies is elusive because of the difficulty in the determination of the continuum edge.

1.3.2 Molecular screening effects on air-suspended tubes

Even for such air-suspended nanotubes, the excitons are known to be screened by adsorbed molecules. The screening effects are more limited when the molecules are desorbed. The spectral changes observed in temperature dependence measurements [46] as well as power-dependent measurements [47, 48] have been attributed to heating induced molecular desorption. More controlled measurements reveal that the adsorbed molecules are water [49], and also molecular dynamics simulations show that the water molecules form a stable double layer on the graphene surface [50], although graphite shows hydrophobicity behavior at the

macroscopic scale. As the molecular adsorption and desorption can nondestructively change the nanotube optical properties, it may be possible to exploit the molecular screening effects to manipulate the excitonic states.

1.4 Research objective

The purpose of this thesis is to elucidate screening effects on excitons in air-suspended carbon nanotubes and explore applications based on the screening effects. For this research objective, we first fabricated air-suspended carbon nanotube field-effect transistors (FETs) and performed simultaneous photocurrent and photoluminescence spectroscopy. Electric-filed effects on excitonic states are investigated on various individual nanotubes with different chirality. In order to investigate molecular screening effects, we have fabricated a system compatible with nitrogen purging and automated sample scanning. The purge system avoids defect formation induced by oxygen and it allows power dependence measurements with high excitation intensities. By using this system, laser-induced molecular desorption effects on emission properties are investigated. Chopper controlled time-resolved measurement system is also constructed to elucidate molecular adsorption and desorption time.

1.5 Organization

In Chapter 2, the device fabrication process of nanotube FETs as well as the measurement setup is described. In Chapter 3, observation of parity forbidden excited excitonic states and continuum states on air-suspended carbon nanotubes are shown. Obtained large binding energies of excitons originated from limited screening of air-suspended tubes are discussed by comparing the previous results on micelle-wrapped tubes. In Chapter 4, we demonstrate all-optical memory operation of single carbon nanotubes by taking advantages of large molecular screening effects on excitons. The switching speed is also elucidated by performing time-resolved measurements.

Chapter 2

Nanotube devices and optical setup

In order to investigate excitonic states via photocurrent (PC) and photoluminescence (PL) spectroscopy, we have fabricated filed effect transistors with air-suspended carbon nanotubes. Here we show how the devices are fabricated and characterized. Details of measurements are also described.

2.1 Fabrication of carbon nanotube field effect transistors

Figure 2.1 shows a schematic of a typical FET device used for PL and PC measurements discussed in Chapter 3. Device fabrication of such devices starts from designing their layout using LayoutEditor. In Figure 2.2, we show a typical design, where 40 independent devices are placed on a chip. The region of the catalyst of each device is designed so that as much as one or few tubes are grown over the trench. The bonding pad is located at the edges of the chip, while the trenches are placed at the center of the chip in order to prevent damages on the tubes due to bonding vibration. This location of the pad also makes it easy to conduct wire bonding.

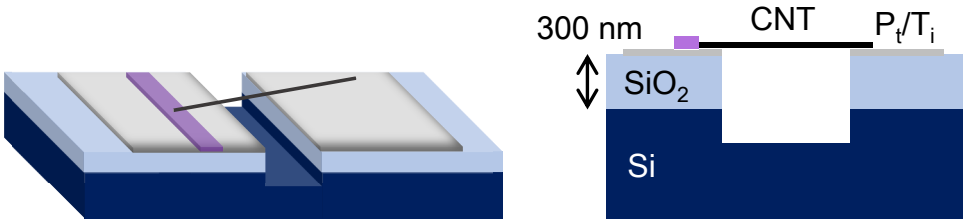

Figure 2.1: A schematic of a carbon nanotube FET device.

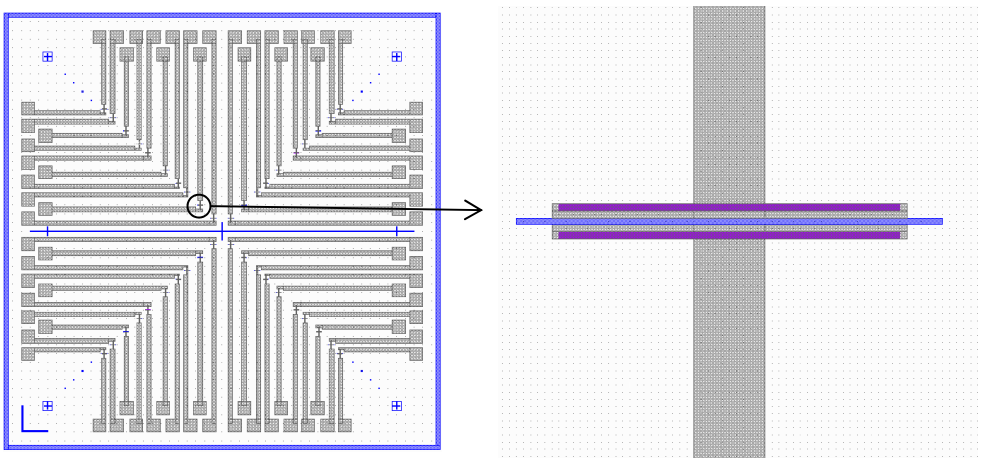

Figure 2.2: Sample layouts. Blue, purple, and gray areas are correspond to trench, electrodes, and catalyst area, respectively.

2.1.1 Micro-fabrication process

We fabricate devices with such a design from silicon wafers. This process begins with micro-fabrication of FETs followed by a carbon nanotube synthesis process. The entire processes flow is summarized in Figure 2.3.

Formation of trenches

(a) A 4-inch Si wafer with 300-nm-thick oxide is cleaned up in acetone by sonication for 10 minutes. The process removes water molecules or dusts on the surface, and allows uniform spin-coating.

(b) Primer (OAP) is spin-coated on the wafer at 3000 rpm for 30 seconds. After that, the wafer is baked at 110°C for 60 seconds on a hotplate. Then a resist

(OEBR CAP-112PM) is spin-coated at 2500 rpm for 60 seconds. Finally, the wafer is baked for 5 minutes at 110°C . As the etching system described later also scrapes off the resist, here we use thick OEBR with a thickness of around 1 μm.
(c) Trench patterns are drawn by electron beam lithography (EBL) with direct exposure. The dose amount is 7 μC/cm^2 and the step and repeat (SR) mode is selected for writing.
(d) The exposed wafer is baked at 110°C for 2 minutes.
(e) The wafer is developed with tetramethyl ammonium hydroxide (TMAH) for 70 seconds then rinsed with water.
(f) The wafer is cut into 30-mm-square chips by a stealth dicer. (This process could be done later).
(g) The chips are dry-etched by an inductively-coupled plasma etcher (ULVAC, CE-300I). Etching gas is CHF_3 and etching time is 200 seconds. This condition forms 500 nm (300-nm SiO_2 and 200-nm Si) deep trenches.
(h) The chips are soaked in remover (Hakuri104) by sonication for 10 minutes. After that, the chips are soaked again in new remover (Hakuri104) by sonication for 10 minutes, and then rinsed with isopropyl alcohol (IPA).
(i) The chips with trenches are annealed in an oxidation furnace at 1050°C with 1.5 L/min O_2 flow for 1 hour. This process removes remaining resists and also form thin silicon oxide on the trenches. The oxide can work as an insulating layer and prevents gate leakage.

Deposition of electrodes

(a) Primer (OAP) and ZEP are spin-coated at 4000 rpm for 60 seconds in this order. After the spin-coating, the chips are pre-baked at 180°C for 15 minutes.
(b) Electrode patterns are written by EBL. The dose amount is 104 μC/cm^2 and SR is selected for writing.
(c) The chips are developed with ZED-N50 for 1 minute, and then rinsed twice with ZMD-B.
(d) 1-nm thick titanium and 30-nm thick platinum are deposited by electron beam evaporator (ULVAC, EX400, Shimoyama group).

(e) The chips are soaked with Hakuri104 by sonication for 5 minutes. After that the chips are soaked again in new Hakuri104 by sonication for 5 minutes, and then rinsed with IPA.
(f) Remaining resists are cleaned up using oxygen plasma ashing for 5 minutes.
(g) The chips are put in acetone by sonication for 5 minutes and then rinsed in IPA for further cleaning.

Patterning of catalyst area

(a) Primer (OAP) and ZEP are spin-coated at 4000 rpm for 60 seconds in this order. After the spin-coating, the chips are pre-baked at 180°C for 15 minutes.
(b) Electrode patterns are written by EBL. The dose amount is 104 μC/cm^2 and SR is selected for writing.
(c) The chips are developed with ZED-N50 for 1 minute, and then rinsed twice with ZMD-B.
(d) The chips are cut into 5-mm-square chips by a stealth dicer.

2.1.2 Synthesis of nanotubes

On the fabricated devices, we synthesize nanotubes, with the following 5 processes. (1) Catalyst preparation, (2) catalyst spin-coat, (3) catalyst lift-off, (4) annealing, and (5) chemical vapor deposition. The details are as follows.

Catalyst preparation

For catalyst solution, 2.5 mg cobalt(II) acetate and 25 mg of fumed silica are dissolved in 10 g ethanol. The fumed silica is dehydrated before use by putting into a drying oven for more than 24 hours. The catalyst solution is mixed with a sonicator for 99 minutes to obtain sufficient dispersion.

Catalyst spin-coat

A drop of catalyst solution is dropped onto a 5-mm chip and spin coated at 5000 rpm for 50 seconds. Then the chips are baked at 150°C for 5 minutes on a

hotplate to dry ethanol. After that, the chip is cooled down to room temperature by putting it on aluminum foil for more than 1 minute.

Catalyst Lift-off

The chips are put into 60 ml remover (Hakuri104) with a magnetic stirrer. The remover is heated to 70°C and the stirrer is rotated at 300 rpm for 40 minutes. Then the chip is rinsed twice with IPA.

Anneal

The chip is annealed in a muffle furnace at 400°C for 5 minutes to remove remaining resists and the organic liquid. The cobalt particles are oxidized in this procedure, which stabilizes nanotube growth.

Chemical vapor deposition

(a) The chip in a quartz boat is put into the quartz tube of the chemical vapor deposition (CVD) furnace.
(b) The pressure in the quartz tube is fixed at 110 kPa while flowing Ar/H_2 gas at 300 sccm. The tube is heated from room temperature to 750°C in 15 minutes, and this condition is kept for 5 minutes to reduce and activate the catalyst metal.
(c) The gas flowing path is switched to the other side where the Ar/H_2 gas passes through liquid ethanol so that carbon source is delivered. This state is kept for 10 seconds. During this short time, nanotubes are grown on the chip. We sometimes use different temperatures for the synthesis process by reflecting on measurement results, because the nanotube yields as well as the diameter distribution depend on the synthesis temperature. In general, as the synthesis temperature approaches 800 degrees, the amount of growth increases, while lower temperatures increases the proportion of short diameter tubes.
(d) We wait 5 minutes until the ethanol vapor flows out, and then cool down the furnace to take out the chip.

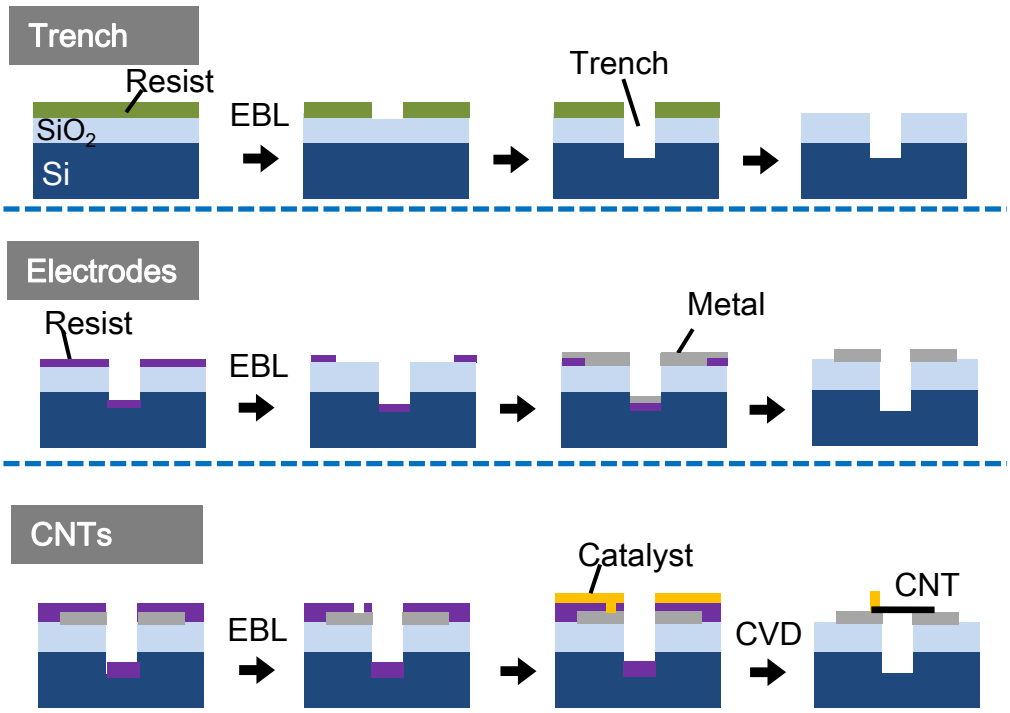

Figure 2.3: Process flow of the device fabrication.

2.2 Measurement setup for photocurrent and photoluminescence spectroscopy

2.2.1 Photocurrent detection with a lock-in amplifier

We use a lock-in amplifier to detect extremely small photocurrent signal from excited excitonic states or continuum states. In order to understand how the sensitive signal detection is realized in the lock-in technique, we consider a simple situation where a signal we want to detect A_0 is on the top of background noise. In such a case, one would modulate A_0 by blocking and unblocking and look at the changes in total signal. Let us consider the situation where the modulation is at a frequency f_0. If we assume broad spectrum noise B_0 and low frequency noise C_0 for the background, and let the frequency of the latter to be zero for simplicity, the total input signal can be expressed as

$$V(t) = \frac{A_0}{2}[1 + \sin(2\pi f_0 t)] + \sum_{f_i \geq 0} B_0 \sin(2\pi f_i t + \phi_i^{rand}) + C_0, \tag{2.1}$$

where ϕ_i^{rand} denotes the random phase of the broad spectrum noise. To extract A_0 from $V(t)$, one might use a bandpass filter centered at the frequency f_0 (Figure 2.4a). This method does not sufficiently lower the S/N ratio, because a quality factor of a bandpass filter are in the order of 100 even for a good one, and a lot of noise with different frequencies are detected. Instead, in a lock-in technique, a low-pass filter is used for noise rejection (Figure 2.4b). To extract only A_0 as a DC component, the input signal is multiplied with reference signal at the same frequency f_0 as

$$\begin{aligned} V(t)V_{ref}(t) &= V(t)\sin(2\pi f_0 t) \\ &= [\frac{A_0}{2}[1+\sin(2\pi f_0 t)] + \sum_{f_i \geq 0} B_0 \sin(2\pi f_i t + \phi_i^{rand}) + C_0]\sin(2\pi f_0 t) \\ &= \frac{A_0}{4} + \sum_{f_i \geq 0} \frac{B_0}{2}[\cos(2\pi(f_i - f_0)t + \phi_i^{rand}) + \cos(2\pi(f_i + f_0)t + \phi_i^{rand})] \\ &\quad + (\frac{A_0}{2} + C_0)\sin(2\pi f_0 t) - \frac{A_0}{4}\cos(4\pi f_0 t). \end{aligned} \tag{2.2}$$

Then the signal is passed through a low pass filter, resulting in obtaining the signal we want. As the bandwidth of the low pass filters are significantly narrow, extremely sensitive signal detection are possible in this technique. Note that we neglected phase differences for simple description. In general, phase shifters are standard in lock-in amplifiers, and the phase differences can be adjusted.

In the actual measurements, we modulate the photocurrent signal at a specific frequency by using optical choppers synchronized to the external reference. The excitation laser is modulated by this optical chopper at 683 Hz, and the both modulated photocurrent signal and the reference signal are connected to the lock-in amplifier (Figure 2.5).

2.2.2 Configuration of measurement system

Simultaneous PC and PL measurements are performed with a home-built sample scanning microscopy system (Figure 2.6) [51]. Wavelength tunable Ti:sapphire laser is used for excitation, and an objective lens with a numerical aperture of 0.8 and a working distance of 3.4 mm focuses the laser onto the sample mounted

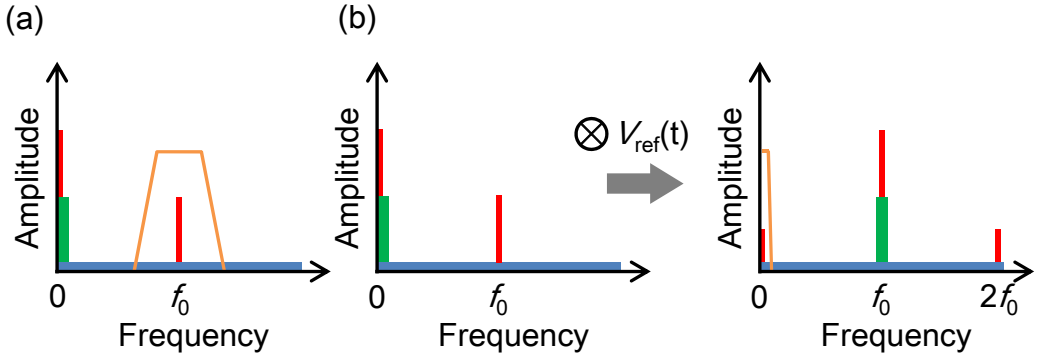

Figure 2.4: Diagrams of lock-in detection. (a) Before mixing. (b) After mixing. Red bars, blue squares, and green bars are showing true signal, broad spectrum noise, and low frequency noise, respectively. The orange curves are indicating band filtering.

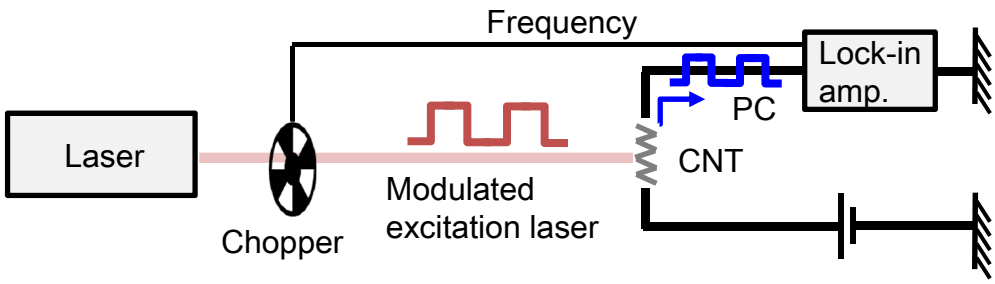

Figure 2.5: Schematic of photocurrent detection using a lock-in amplifier.

on the 3D stage. We use a continuously variable neutral-density (ND) filter on the transition stage to control the excitation power. The linear polarization of the laser can be rotated using a half-wave plate placed immediately before the lens, and an optical chopper in the excitation path modulates the laser intensity at 683 Hz. We use a lock-in amplifier to eliminate low-frequency noise and to achieve sensitive detection of PC. The source contact is connected to a virtual ground input of the lock-in, and a bias voltage V is applied to the drain contact to establish an electric field $F = V/w$ where w is the width of the trench. In order to avoid PL quenching caused by electrostatic doping, we also apply $V/2$ to the Si substrate to keep the effective gate voltage at the center of the tube to be zero. PL is collected through a confocal pinhole, and an InGaAs photodiode array

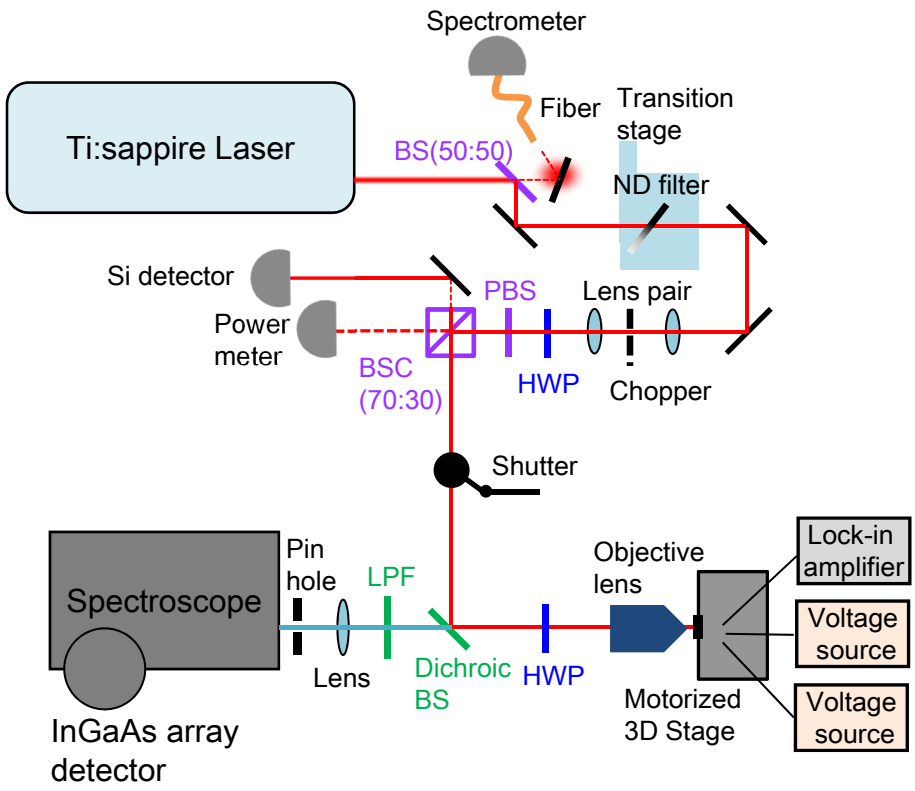

Figure 2.6: A schematic of an optical setup.

attached to a spectrometer is used for detection. Because actuators are attached on optical elements as well as the transition stage, not only the applied voltage but also the excitation wavelength, power, polarization, and the sample position can be controlled by a computer. In addition, since all controls are performed via home-build LabVIEW programs, flexible automatic measurements are possible by writing appropriate programs.

2.3 Characterization of nanotube devices

2.3.1 Optical measurement to find air-suspended nanotubes

PL line scans are performed for all devices on the chip to find air-suspended tubes [52]. Typically, 710, 777, and 850 nm, are used for excitation, as there are a lot of tubes resonant to these excitation wavelengths. By comparing the

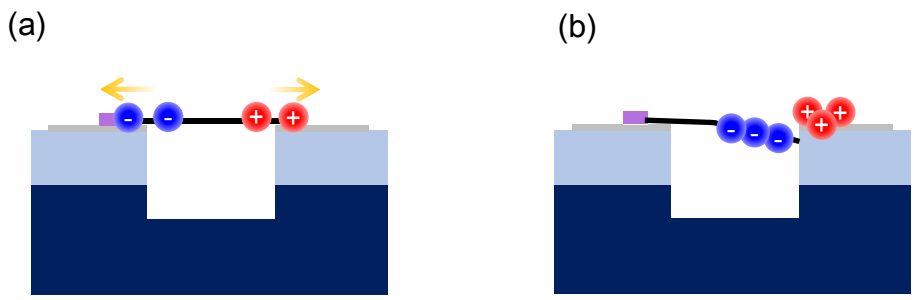

Figure 2.7: A schematic of (a) fully suspended and (b) partially suspended nanotube under bias voltage.

emission wavelength with tabulated data [52], we roughly assign the chirality of the nanotubes.

We then connect the terminals of the chip carrier to the electrodes of the nanotube FETs, which show bright PL but do not show dark current. A manual wire bonder is used for this connection. We note that some tubes are partially suspended and not contacted properly to both electrodes . Although PL can be observed, this type of tubes do not show PC signal, rather they exhibit quenching behavior under weak bias. The bias can cause carrier accumulation and this leads to PL quenching if the tubes are partially connected, because contacted electrodes define the Fermi level of the tube, while the other electrode can work as a gate (Figure 2.7b).

2.3.2 Sample tracking for stable optical measurement

In every precise measurement, we perform fine sample alignment. As the excitation spot of our optical setup is around 1 micron, just half a micron of a sample drift can significantly reduce the PL and PC signals. We therefore track a nanotube by a program that automatically measures the sample position. Reflectivity measurement in the y axis direction is used for finding the center of the trench and tubes, while PL 1D scan in the x and z axes identify the precise position of the nanotube (Figure 2.8).

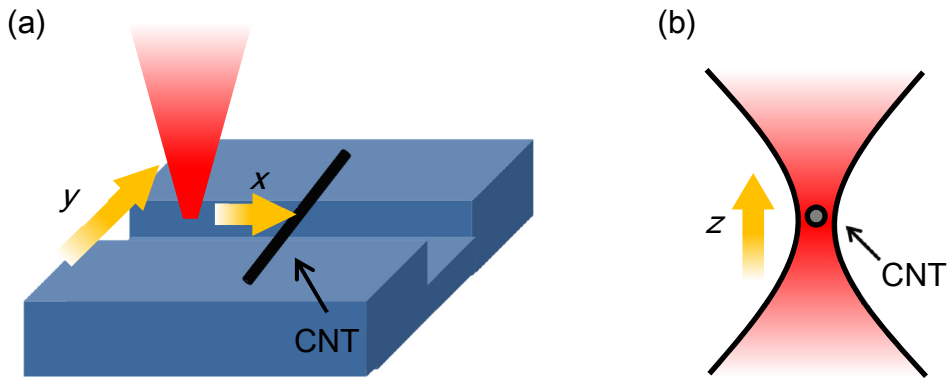

Figure 2.8: A schematic of sample alighment for (a) y, x and (b) z direction.

Chapter 3

Limited screening of excitonic states in air-suspended carbon nanotubes

Here we investigated how the Coulomb interactions are enhanced in the air-suspended nanotubes, by performing simultaneous PC and PL excitation spectroscopy on nanotube devices shown in Chapter 2. As the applied field on the devices are increased, we observe an emergence of new absorption peaks in the excitation spectra. From the diameter dependence of the energy separation between the new peaks and the ground state of E_{11} excitons, we attribute the peaks to the dark excited states which became optically active due to the applied field. Field-induced exciton dissociation can explain the photocurrent threshold field, and the edge of the E_{11} continuum states has been identified by extrapolating to zero threshold. By comparing the edge with the emission energy, we obtain the significantly large binding energy of excitons, exhibiting the particularly limited screening in the air-suspended nanotubes.

3.1 Dark excitonic states

The strong Coulomb interactions due to the limited screening in quasi-one dimensional structure of nanotubes result in optical spectra dominated by tightly bound excitons with binding energies of more than a few hundred meV [2,22,23,25]. The

excitons have a series of excited states in a manner similar to the Rydberg states in atomic hydrogen, and they have either odd (u) or even (g) parity because of the K and K' valleys in the momentum space being equivalent [24–26, 29]. Since one-photon transitions require a parity change, the odd excitonic series ($1u$, $2u$, $3u$,...) are bright, while the even excitonic series ($1g$, $2g$, $3g$,...) are dipole-forbidden dark states [24, 26, 29].

These dark states have been studied by two-photon excitation spectroscopy that allows for same-parity transitions [23, 24, 26], and photoluminescence (PL) measurements under strong magnetic fields have been used as well [30, 32–34]. It is expected that electric fields also cause the dark states to become optically active because of wave function mixing [53], and it gives rise to interesting phenomena such as exciton dissociation, Stark shift, and Franz-Keldysh oscillations [54–61]. In particular, the activation of the dark states could be a key to developing efficient nanotube-based photodetectors and photovoltaic devices, but a well-controlled experiment has been lacking. Although electroabsorption spectra have been interpreted by state-mixing effects [62], complicated spectra for an ensemble of nanotubes result in large uncertainties. Spectral diffusion has been attributed to impurity-induced fields [35], while their fluctuating nature makes it difficult to draw quantitative conclusions.

3.2 Observation of parity forbidden excited excitonic states

3.2.1 Bias induced peaks

Our measurements are performed on field-effect transistors with individual air-suspended nanotubes (Figure 3.1b), for which we described the fabrication process in Chapter 2. We first perform PL excitation spectroscopy at $F = 0.00$ V/μm to determine its chirality. In Figure 3.1a, a PL excitation map for a nanotube in a typical device is shown, where an excitation laser power $P = 10$ μW is used. We assign the chirality by comparing the E_{11} and E_{22} energies to tabulated data [52], and confirm that both of the values differ by less than 10 meV. Simul-

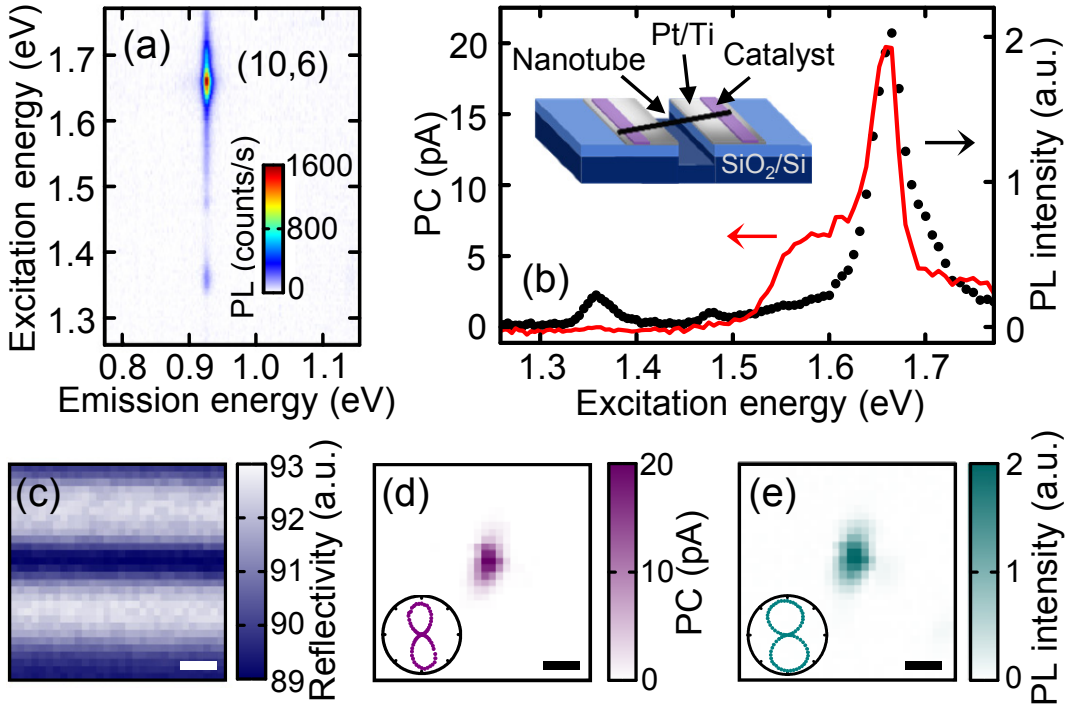

Figure 3.1: Optical characterization of a (10,6) nanotube in a device with $w = 0.6$ μm. Excitation power is 10 μW and laser polarization is parallel to the nanotubes axis unless otherwise noted (a) A PL excitation map measured with $F = 0.00$ V/μm. (b) PC (red curve) and PL (black dots) excitation spectra. PL intensity is obtained by fitting the emission spectra with Lorentzian functions and calculating the peak area. Inset is a schematic of the device. (c), (d), and (e) are reflectivity, PC, and PL images, respectively. The scale bars are 1 μm. Insets in (d) and (e) are the laser polarization angle dependence of the PC and PL intensity, respectively. (c-e) are measured at an excitation energy of 1.66 eV. (b-e) are measured at $F = 0.33$ V/μm. We note that PL polarization dependence is less pronounced compared to PC because of exciton-exciton annihilation effects [48, 52, 54]. Original data presented in Ref. [51].

taneously measured PC and PL excitation spectra (Figure 3.1b) at a low electric field of $F = 0.33$ V/μm confirm that the E_{22} absorption resonance occurs at an identical energy of 1.66 eV, while imaging measurements (Figure 3.1c-e) ensure that both signals are spatially coincident at the trench. Polarization dependence (Figure 3.1d,e insets) is used to determine the angle of the nanotube [48], and we confirm that both PC and PL show consistent behavior. These procedures ensure that the signals arise from the same individual nanotube.

After such careful characterization, electric field dependence of PC and PL excitation spectra are investigated (Figure 3.2). Three PL excitation spectra measured at different electric fields are shown in Figure 3.2a, and a more de-

tailed electric field dependence taken from $F = 0.00$ to 10.00 V/μm is shown in Figure 3.2b. The most prominent peak observed at 1.66 eV corresponds to the E_{22} exciton ground state, which does not show much field dependence. In the spectrum obtained at $F = 0.33$ V/μm (Figure 3.2a, gray curve), we observe two weaker peaks at 1.36 eV and 1.48 eV which can be assigned to the $2u$ and $3u$ states, respectively [24, 25]. When the applied electric field is increased to $F = 3.33$ V/μm, the peak for the $3u$ state disappears (Figure 3.2a, blue curve), and with further increase to $F = 8.33$ V/μm, the peak for the $2u$ state shows a redshift and a considerable reduction in its height (Figure 3.2a, red curve). The behaviors of $2u$ and $3u$ states are much more sensitive to the electric field, in contrast to the E_{22} exciton peak.

In PC spectra, more significant changes are observed (Figure 3.2c,d). Under the weakest electric field of $F = 0.33$ V/μm, only the E_{22} exciton ground state is observed (Figure 3.2c, gray curve). When the applied electric field is increased to $F = 3.33$ V/μm, a new peak appears at 1.50 eV (Figure 3.2c, blue curve). This peak is close to but different from the $3u$ state (Figure 3.3), and is denoted as X^* in Figure 3.2c. As the electric field is increased (Figure 3.2d), we observe a blueshift of the X^* peak and an emergence of another lower energy peak which we will refer to as the X peak. At $F = 8.33$ V/μm, the X^* peak and the X peak can be seen at 1.56 eV and 1.39 eV, respectively (Figure 3.2c, red curve). We note that the X peak can also be observed in the PL excitation spectra as a faint peak (Figure 3.2b, Figure 3.4).

A conceivable explanation for the X and X^* peaks is that they are the parity-forbidden dark excited states. Since electric fields cause wave function mixing [35, 53, 62], the dark states can become optically active. If these states dissociate into free carriers by the field, peaks can appear in the PC spectra. The X and X^* peaks show up near the $2u$ and $3u$ states, suggesting that they correspond to the $2g$ and $3g$ states, respectively.

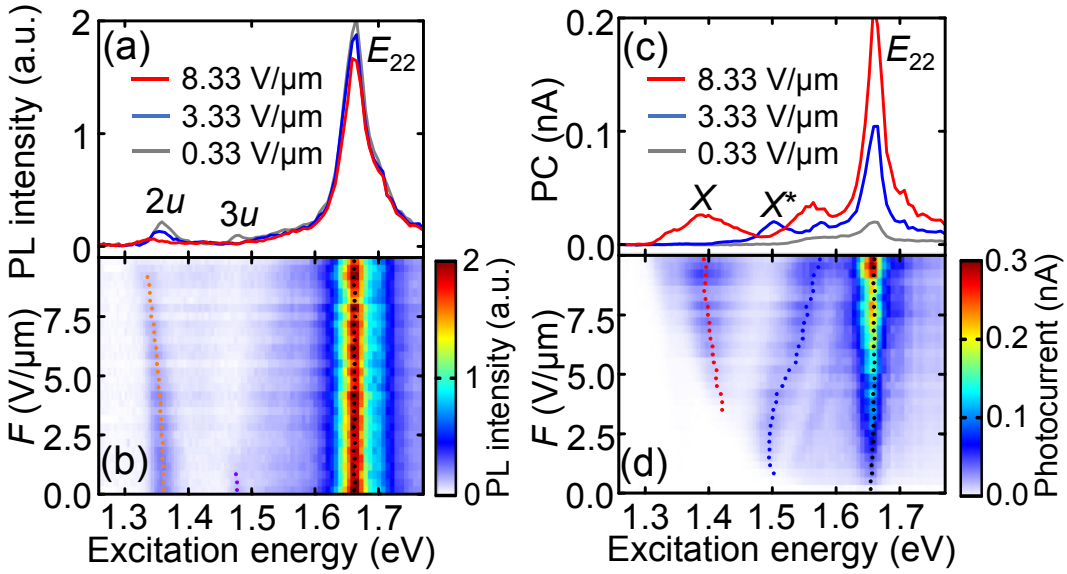

Figure 3.2: The nanotube characterized in Figure 3.1 is measured with $P = 10$ μW. The laser polarization is parallel to the nanotubes axis. (a) and (c) are PL excitation and PC spectra, respectively, measured at $F = 0.33$ V/μm (gray), $F = 3.33$ V/μm (blue), and $F = 8.33$ V/μm (red). (b) and (d) are electric field dependence of PL excitation and PC spectra, respectively, taken from $F = 0.00$ to 10.00 V/μm with 0.33 V/μm step. The orange, purple, red, blue, and black dots indicate spectral peak positions for the $2u$, $3u$, X, X^*, and E_{22}, respectively. Original data presented in Ref. [51].

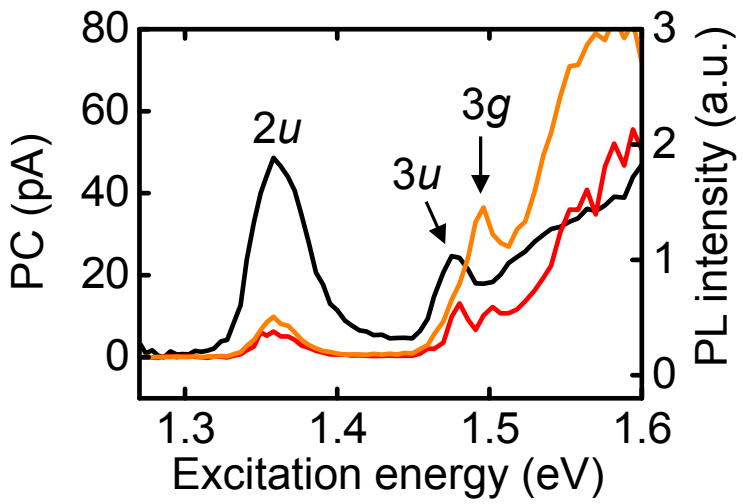

Figure 3.3: The same nanotube as in Figure 3.1-3.5 is measured under $P = 100$ μW. Red and orange curves are PC spectra measured at $F = 0.33$ and 0.67 V/μm, respectively. Black curve is a PL excitation spectrum measured at $F = 0.33$ V/μm. Original data presented in Ref. [51].

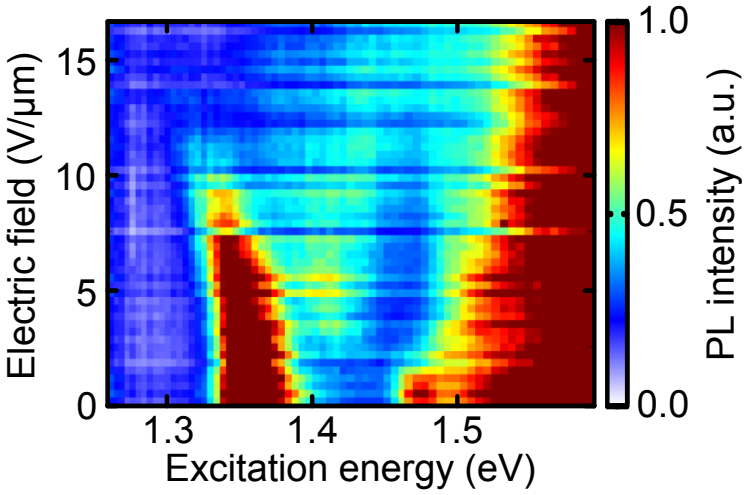

Figure 3.4: Electric field dependence of PL excitation spectra taken from $F = 0.00$ to 16.67 V/μm with 0.33 V/μm step. The nanotube is the same as in Figure 3.1-3.5, and $P = 100$ μW is used. The X peak can be seen at 1.41 eV around $F = 5$ V/μm. Original data presented in Ref. [51].

3.2.2 Electric-field dependence

In order to examine if such a picture is reasonable, a more detailed quantitative analysis is performed. We fit each peak in the PL excitation and PC spectra in Figure 3.2b,d by using a Lorentzian plus a linear function, and plot the electric field dependence of the peak heights and positions in Figure 3.5. First we discuss the changes in the normalized PL intensity (Figure 3.5a). As the field increases to $F = 10.00$ V/μm, E_{22} excitation results in only about 20% decrease while $2u$-state excitation shows a reduction to about one quarter, again highlighting the sensitivity of the excited states to electric fields. In the electric field dependence of the peak PC, different dissociation behaviors are observed for the various peaks (Figure 3.5c). PC increases linearly without a threshold for E_{22} excitation, indicating that built-in electric fields are negligible and excitons are spontaneously dissociating [54]. In the case of X and X^* peaks, however, we observe thresholds at $F = 3.33$ V/μm and 0.67 V/μm, respectively, showing that electric fields are necessary for dissociation of the underlying states. The X^* peak shows a higher PC compared to the X peak, which may be due to either larger absorption cross section or more efficient dissociation.

Next we discuss the energy shifts of the peaks in the PL excitation and PC

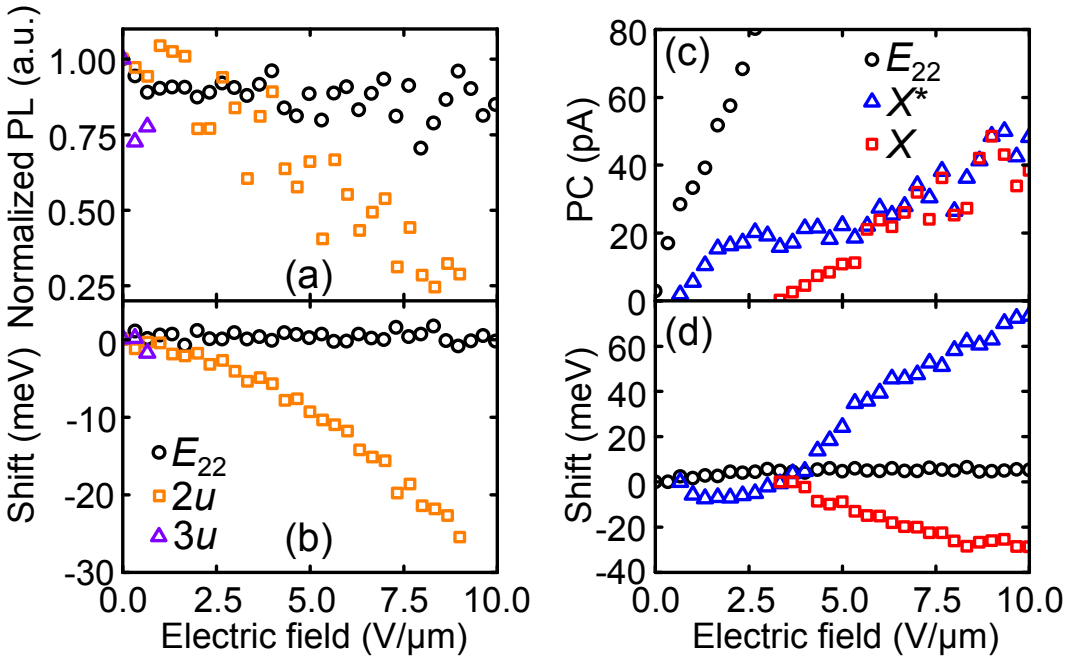

Figure 3.5: Fitting results of various peaks in Figure 3.2b,d by using a Lorentzian plus a linear function. (a) and (c) Electric field dependence of peak heights in the PL excitation and PC spectra, respectively. For (a), PL intensities are normalized at $F = 0.00$ V/μm. (b) and (d) Electric field dependence of energy shifts for the peaks in the PL excitation and PC spectra, respectively. The shifts for the E_{22}, $2u$, $3u$, X^*, and X are measured from 1.662, 1.361, 1.477, 1.502, and 1.421 eV respectively. Original data presented in Ref. [51].

spectra (Figure 3.5b,d). The peak position of the E_{22} excitons do not shift so much which is similar to the behavior of $1u$ state of E_{11} excitons [59], while the $2u$ state shows a large Stark shift of about 30 meV at $F = 10.00$ V/μm. This is expected as the excited states generally have larger sizes compared to the ground states, and therefore they are more responsive to the applied field. Similar to the $2u$ state, the X and X^* peaks also show large shifts of about 30 and 70 meV, respectively, consistent with the interpretation that the X and X^* peaks are the excited states. We note that the dispersions of the peak shifts show different behaviors, which may be caused by complicated mixing of various excitonic states such as K-momentum states and the E_{22} state as well as the E_{11} continuum.

3.2.3 Diameter dependence

To obtain additional data that support the assignment of the X and X^* peaks, we perform PC and PL excitation measurements on various individual nanotubes

with different chiralities. Three typical PC spectra that show the X peaks are plotted in Figure 3.6a-c. No correlation between the X and E_{22} peaks are observed, showing that they are not a sideband of E_{22} excitons. We fit such spectra using Lorentzian functions and plot the energy difference between the various peaks and the $1u$ state as a function of the tube diameter d in Figure 3.6d. The energy separations for the bright excited states ($2u$ and $3u$ states) are inversely proportional to d, as observed previously [25]. The inverse proportionality is a characteristic of the excited states [63], and similar dependence has also been observed for the $2g$ states [64]. We find that the X and X^* peaks also show such a dependence, indicating that the peaks arise from the excited states of E_{11} excitons. It is noted that these peaks cannot be observed in the absence of the electric fields, for all of the chiralities investigated. In addition, the X peak always appears at an energy higher than the $2u$ state but lower than the $3u$ state, and the X^* peak shows up slightly above the $3u$ state for all nanotubes. These results confirm our interpretation that the X and X^* peaks are the $2g$ and $3g$ states of E_{11} excitons, respectively.

3.3 Enhancement of Coulomb interactions in suspended nanotubes

3.3.1 Comparison with micelle-wrapped tubes

The assignment is consistent with previous work on the dark states that used micelle-wrapped tubes. The $2u$ states are observed at 200 meV above the $1u$ states by one-photon measurements, while two-photon excitation measurements have shown that the energy difference between the $2g$ states and the $1u$ states is 240 meV [24]. Since our nanotubes are air-suspended and environmental dielectric screening is weaker, enhancement of the energy separation is expected [27, 65]. Indeed, we observe the $2u$ states and the $2g$ states (X peaks) at 470 and 540 meV above the $1u$ states, respectively, for $d = 1.00$ nm tubes (Figure 3.6d). These results are consistent with the dielectric constant scaling obtained for air-ambient nanotubes [25]. Note that the X peaks are typically identified at $F = 5.0$ V/μm

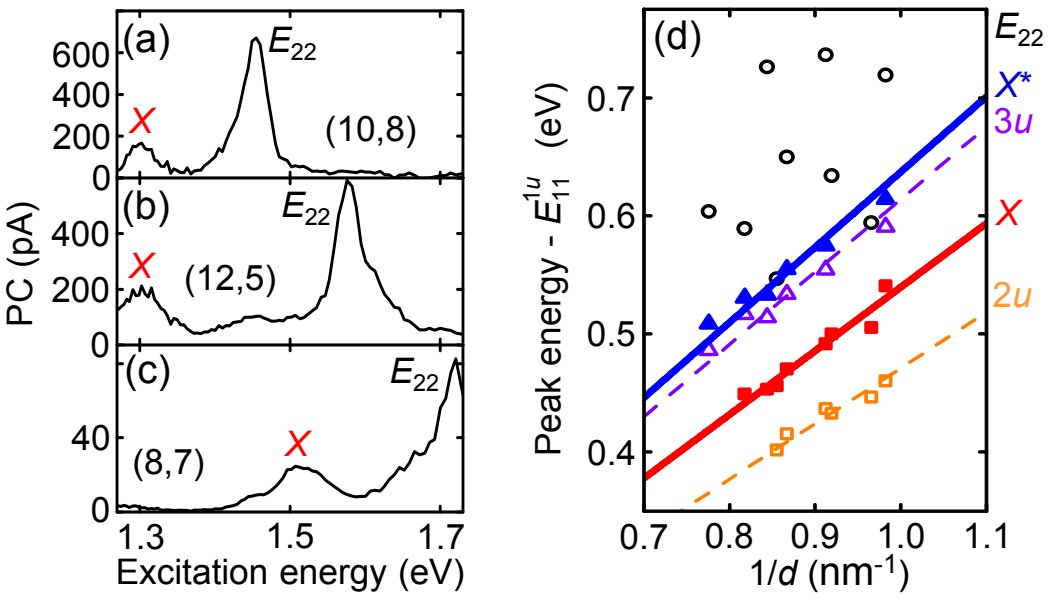

Figure 3.6: (a) PC spectrum for a (10,8) nanotube measured with $F = 5.94$ V/μm and $P = 10$ μW. (b) PC spectrum for a (12,5) nanotube measured with $F = 8.75$ V/μm and $P = 10$ μW. (c) PC spectrum for a (8,7) nanotube measured with $F = 11.67$ V/μm and $P = 5$ μW. (d) Diameter dependence of the energy separation from the $1u$ states for $2u$ (orange open squares), X (red filled squares), X^* (blue filled triangles), $3u$ (purple open triangles), and E_{22} (black open circles). The X and X^* peak positions are identified using PC spectra at the weakest electric field where they can be observed. Typical fields are $F = 5.0$ and 1.5 V/μm for the X and X^* peaks, respectively. For the bright excitonic states, PL excitation spectra taken with $F < 0.20$ V/μm are used. Lines show linear fits with zero intercept, and the slopes are 471, 540, 614, and 637 meV·nm for $2u$, X, $3u$, and X^*, respectively. Original data presented in Ref. [51].

where redshifts of about 20 meV have occurred. Taking into account such shifts, the ratio of the energy separations is comparable to the micelle-wrapped tubes, while due to the difference in the environmental screening, the energies are about twice as much.

3.3.2 Exciton dissociation

We now turn our attention to PC threshold fields for the $2g$ (X) and $3g$ (X^*) states (Figure 3.5c), and show that they can be explained by field-induced exciton dissociation. In the presence of electric fields, bound excitons can tunnel into the continuum, and the dissociation threshold field scales as $E_b^{3/2}$ where E_b is the exciton binding energy [60]. The relatively large threshold field observed for

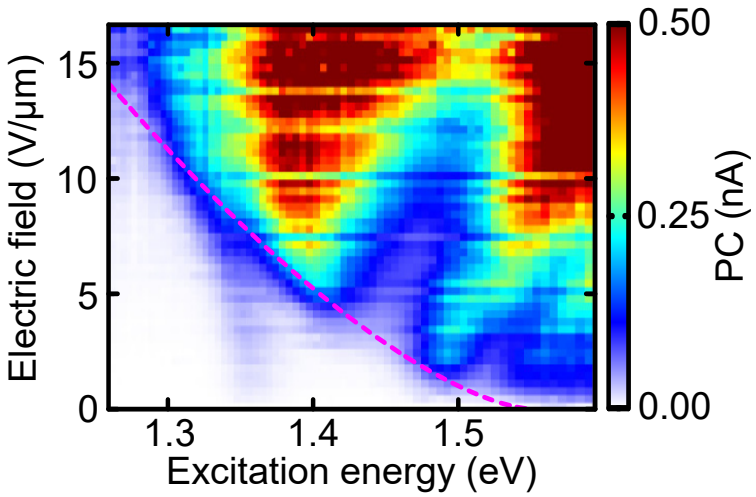

Figure 3.7: Electric field dependence of PC spectra taken from $F = 0.00$ to 16.67 V/μm with 0.33 V/μm step. The nanotube is the same with Figure 3.1-3.5, and $P = 100$ μW is used. Pink dotted curve shows $E_{\mathrm{b}}^{3/2}$ dependence of the boundary. Original data presented in Ref. [51].

the $2g$ (X) state can be attributed to its lager binding energy, and in general excited states farther away from the continuum should show higher thresholds. Indeed, in Figure 3.2d, the boundary between the blue region and the white region shows such a dependence as expected (also see Figure 3.7). The dissociation mechanism is similar to the ionization of a hydrogen atom in a field [66], but with binding energies that is two orders of magnitude smaller. In comparison to bulk semiconductors, the ground state binding energy is more than an order of magnitude larger, allowing for spectroscopic study of the excited states.

3.3.3 Exciton binding energies

Based on this analysis, we consider the point where the dissociation field becomes zero which should correspond to the edge of the continuum states. For the tube shown in Figure 3.2d, it is located at 1.55 eV, and the PC spectrum measured at the lowest electric field (Figure 3.1b) shows a shoulder above this energy. As the excited states of E_{11} excitons are lower in energy compared to the shoulder, it is reasonable to interpret this spectral feature as the E_{11} continuum states. Similar features are observed in other nanotubes with different chiralities (Figure 3.8), supporting the interpretation. We note that the continuum states can only be observed clearly in certain chiralities whose E_{22} excitons are sufficiently sepa-

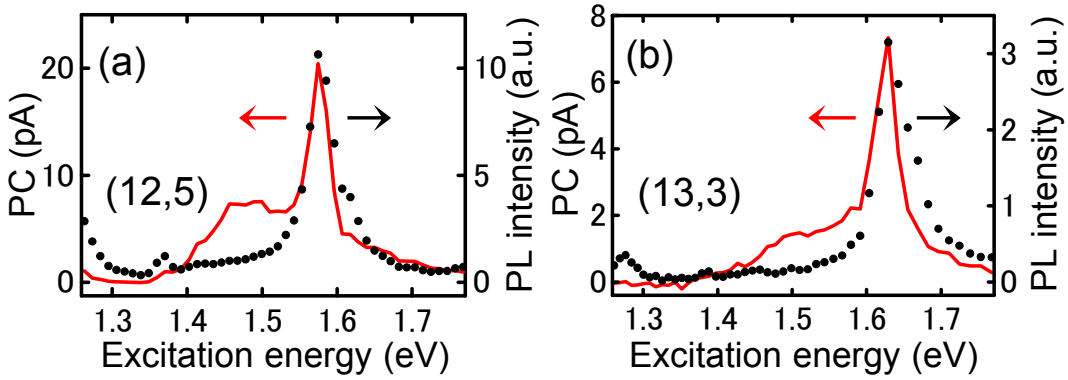

Figure 3.8: PC (red curve) and PL excitation (black dots) spectra obtained at low electric fields, which show the continuum states as shoulders. (a) Spectra for a (12,5) nanotube measured with $F = 0.13$ V/μm and $P = 10$ μW. (b) Spectra for a (13,3) nanotube measured with $F = 0.10$ V/μm and $P = 10$ μW. Original data presented in Ref. [51].

rated from the continuum edge. The direct identification of the continuum edge has been difficult in carbon nanotubes because most of the oscillator strength is transferred to excitonic resonances. In spite of such an effect, PC spectroscopy provides a way to determine the edge because of the zero dissociation fields.

As the PL emission energy indicates the energy level of the exciton ground state, we now able to obtain the exciton binding energy by taking the difference between the emission energy and the continuum edge. We observed PL peak at 0.930 eV with $F = 0.00$ V/μm (Figure 3.1a) , while the energy of continuum edge obtained by extrapolating the zero threshold field is located at 1.55 eV. We therefore obtain exciton binding energy of 620 meV for this nanotube, which is 1.5 times larger than the estimation for micelle-wrapped tubes [23, 24].

3.4 Summary

In summary, we have investigated the electric field dependence of various excitonic states in individual suspended carbon nanotubes by simultaneously measuring both PC and PL. As fields are increased, optical transitions to the parity-forbidden dark states of E_{11} excitons are activated. The clear diameter dependence of the peak energies has been used to assign them to the $2g$ and $3g$ states. Comparison with the previous work on the dark states that used micelle-wrapped

shows that the environmental screening changes the excitonic energies by more than a factor of 2. Furthermore, we have observed PC threshold fields that can be explained by field-induced exciton dissociation, and a shoulder in the PC spectra have been identified as the E_{11} continuum states. By subtracting the PL emission energy from the assigned continuum edge, we obtain as large as 620 meV exciton binding energy. Our results highlight the significantly large Coulomb interactions enhanced in the suspended nanotubes.

Chapter 4

Exciton manipulation with screening effects induced by adsorbed molecules

In Chapter3, we have discussed the pronounced screening effect on excitonic energies in carbon nanotubes, and also show how the screening is reduced in the air-suspended nanotubes. Even such suspended nanotubes, however, adsorbed molecules on their surface are functioning as a screening medium. Here we exploit these molecular screening effects on excitons to control the emission properties by optical means, and show that adsorbed molecules give rise to optical bistability. By exciting at the high-energy tail of the excitonic absorption resonance, nanotubes can be switched between the desorbed state and the adsorbed state. We demonstrate reversible and reproducible operation of the nanotube optical memory, and determine the rewriting speed by measuring the molecular adsorption and desorption times.

4.1 All-optical memories based on air-suspended nanotubes

On-chip photonic devices can potentially boost the capabilities of modern information-processing systems by replacing their electrical counterparts, as they offer a number of advantages such as low power dissipation, high speed processing, and re-

duced crosstalk [67]. High-efficiency photon generation can be achieved with thresholdless lasing in nanoscale metallic cavities [68], while terahertz modulation has been accomplished using silicon-polymer hybrid waveguides [69]. Further development towards optical computing requires advances in key devices such as all-optical memories and switches. These functional devices usually employ optical bistability, where two optically distinguishable states can be selected by optical means [70]. The majority of the optical bistable devices rely on cavity effects [71–76], since they provide strong light confinement for enhancing nonlinearity and allow miniaturization of the systems. Even the smallest cavities, however, have length scales of a few microns needed to confine the light waves, putting a limit to size reduction. Another route for high-density integration of optical memories and switches is the use of nanomaterials that exhibit optical bistability.

Single-walled carbon nanotubes (CNTs) are appealing for such applications because they can be integrated with silicon photonics [10, 11, 77] and their optical properties have unique characteristics [78, 79]. With the atomically-thin structures, weak dielectic screening results in tightly bound excitons dominating the optical transitions even at room temperature [2, 23, 24]. The excitonic energies are structure dependent, offering resonances throughout the telecommunication wavelength [17], while one-dimensionality gives rise to linearly polarized selection rules [80]. By using a suitable combination of wavelength and polarization, individual CNTs can be addressed, providing access to ultrasmall volumes [81]. Since environmental screening plays an important role in determining the excitonic levels [18, 82], suspended CNTs show a considerable modification of the transition energies even with water molecule adsorption [25,46,49,83]. Excitation-power-dependent photoluminescence (PL) emission energy has been attributed to heating-induced molecular desorption [47, 48], suggesting that optical control of CNT emission properties is possible via the adsorbed molecules.

Here we report on optical bistability in individual carbon nanotubes, arising from excitonic resonance shifts induced by molecular adsorption and desorption. Power dependence measurements show that the nanotubes can take two different

emission states under the same excitation condition, and the optical bistability is only observed for excitation energies sufficiently higher than the excitonic absorption peak characteristic of CNTs. We find that shifting of the E_{22} resonance can explain the hysteresis, where a large difference in the laser heating efficiency for the two states results in different threshold powers. We employ the bistability to demonstrate reversible and reproducible switching operation, and perform time-resolved measurements to determine the rewriting speed of the nanotube optical memory.

4.2 Optical bistability

4.2.1 Sample and measurement system

Our samples are individual CNTs suspended over trenches on silicon substrates (Figure 4.1). Fabrication process is a similar but slightly different from the devices that used in the previous chapter [84]. Briefly, electron beam lithography and dry etching processes are performed on bare Si substrates to form the trenches, and catalyst areas are patterned by an additional electron beam lithography step. Fe(III) acetylacetonate and fumed silica dispersed in ethanol are spin-coated as catalysts, and single-walled carbon nanotubes are grown over the trenches by alcohol chemical vapor deposition from catalyst particles placed near the trenches.

After such fabrication processes, we put the samples in the same PL microscopy system used in the previous chapter (Figure 2.6), but this time the samples are kept in nitrogen to prevent formation of oxygen-induced defects [85, 86] (see Appendix A). We note that the samples have been exposed to atmosphere during transfer from the synthesis furnace to the optical system.

4.2.2 Optical bistability in air-suspended nanotubes

A typical PL excitation map of an individual nanotube measured with a laser power $P = 2$ μW is shown in Figure 4.2a. Clear resonances of emission and excitation are observed, which correspond to the E_{11} and E_{22} energies, respectively. By comparing these energies to tabulated data [52], we assign the chirality of the

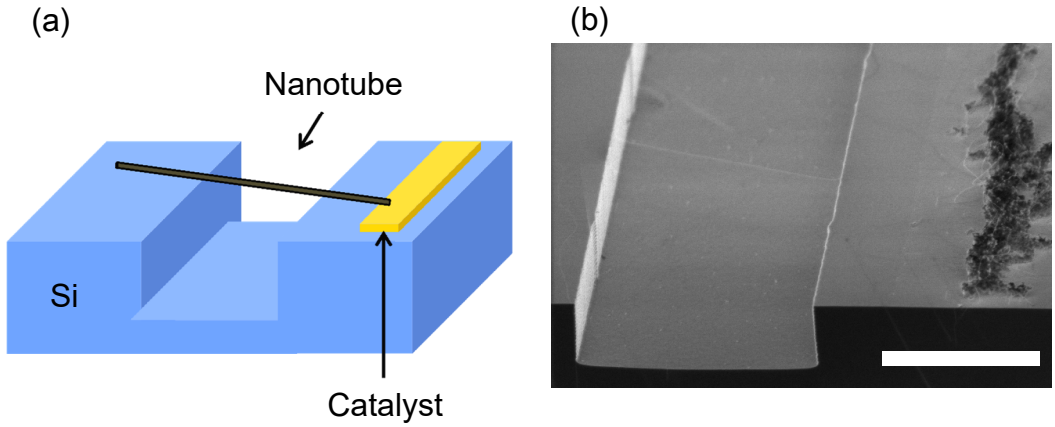

Figure 4.1: (a) A schematic and (b) a scanning electron microscope image of a sample. An original picture presented in Ref. [84].

nanotube to be (10, 5).

In Figure 4.2b, we show PL spectra of this nanotube taken at $P = 700$ μW during an up sweep (red curve) and a down sweep (blue curve) of the excitation power, where an excitation energy $E_{\text{ex}} = 1.644$ eV is used. The spectrum for the up sweep shows a peak at 1.025 eV, which is close to the emission energy in the PL excitation map. For the down sweep, however, we observe a single peak at a much higher energy of 1.047 eV.

4.2.3 Energy detuning dependence

In order to understand the origin of the different emission states, detailed excitation power dependence of PL emission spectra is measured. In the up sweep (Figure 4.2c), an abrupt spectral change is observed at $P = 870$ μW, which is attributed to the laser-heating induced molecular desorption [47, 48]. Interestingly, we find that the abrupt spectral change occurs at a much lower power of $P = 570$ μW for the down sweep (Figure 4.2d). The hysteretic behavior immediately indicates the presence of optical bistability [70], as the nanotube takes two different emission states depending on its excitation history.

We have performed such excitation power dependence measurements for various detuning energies $\Delta E_{\text{ex}} = E_{\text{ex}} - E_{22}$ to investigate the mechanism of the bistability, and typical up-sweep data are plotted in Figure 4.3a-c. When we

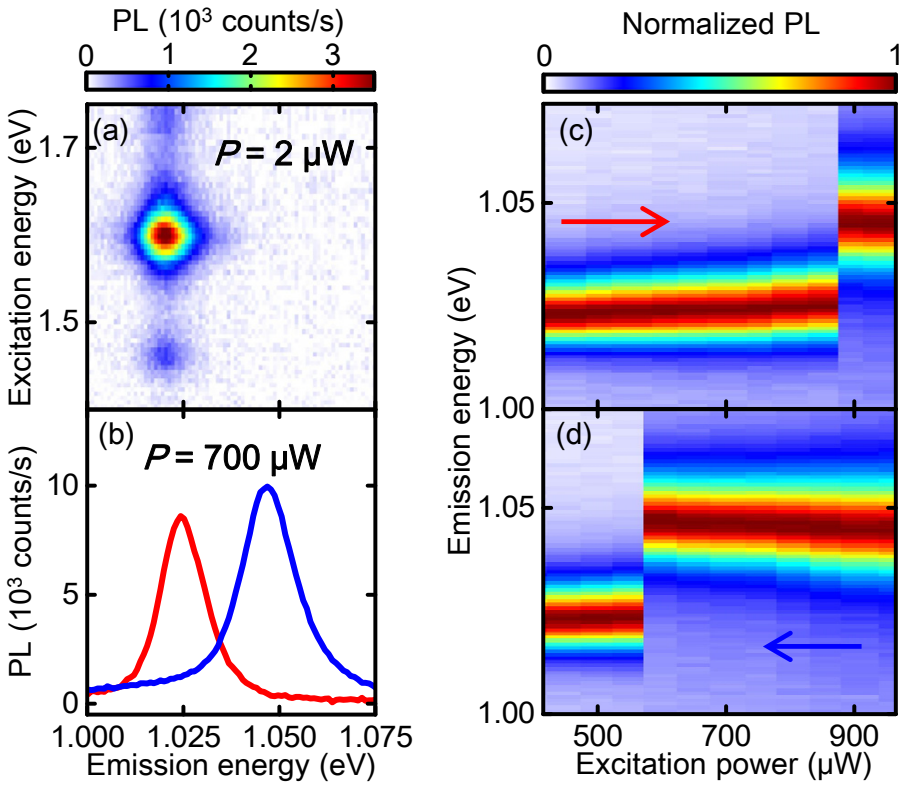

Figure 4.2: Optical bistability of an individual CNT. (a) A PL excitation map of a 2.38-μm-long (10,5) nanotube taken with $P = 2$ μW, showing an emission peak at 1.021 eV and an excitation resonance at 1.603 eV. The inset is a schematic of a sample. (b) PL spectra measured at $P = 700$ μW during an up sweep (red curve) and a down sweep (blue curve). (c) and (d) Excitation power dependence of normalized PL spectra for an up sweep and a down sweep, respectively. The spectra are normalized by the maximum intensity at each power. All data are taken with laser polarization parallel to the tube axis, and $\Delta E_{\text{ex}} = +41$ meV is used in (b-d). Original data presented in Ref. [84].

excite the nanotube with $\Delta E_{\text{ex}} = -3$ meV, the spectrum shows a continuous blueshift as the excitation power increases (Figure 4.3a). The smooth spectral shift implies that the adsorbed molecules are gradually desorbing by laser-induced heating. As the excitation energy is increased to $\Delta E_{\text{ex}} = +9$ meV, the spectrum shows a more abrupt blueshift (Figure 4.3b), and a discontinuous blueshift is observed at a much higher energy of $\Delta E_{\text{ex}} = +28$ meV (Figure 4.3c).

In Figure 4.3d, we show both the up- and down-sweep power dependence of the emission energy measured at these three detuning energies. Hysteresis is not observed at relatively small detunings of -3 meV and $+9$ meV, while a clear hysteresis loop opens up for the large positive detuning energy of $+28$ meV. The

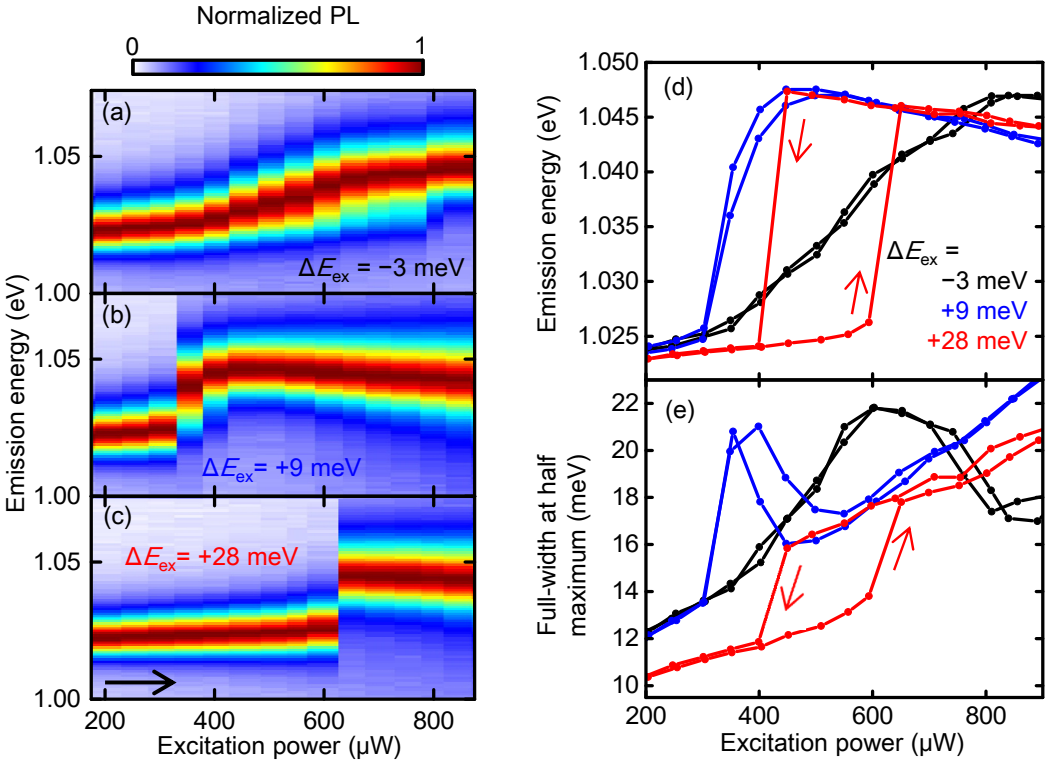

Figure 4.3: Detuning energy dependence of the spectral transitions. Excitation power dependence of the normalized PL spectra taken with (a) $\Delta E_{\mathrm{ex}} = -3$ meV, (b) $\Delta E_{\mathrm{ex}} = +9$ meV, and (c) $\Delta E_{\mathrm{ex}} = +28$ meV. The spectra are normalized by the maximum intensity at each power. Excitation power dependence of (d) emission energy and (e) full-width at half-maximum, obtained by fitting the PL spectra with a Lorentzian function. The detuning energies of -3 meV (black), $+9$ meV (red), and $+28$ meV (blue) are used. Broadening observed around $P = 600$ μW for $\Delta E_{\mathrm{ex}} = -3$ meV and near $P = 400$ μW for $+9$ meV in (e) are artifacts caused by the overlap of the emission peaks from the adsorbed and desorbed states. All data are taken with laser polarization parallel to the tube axis. Original data presented in Ref. [84].

hysteretic behavior presented in Figure 4.2c,d have also been taken with a large detuning of +41 meV, suggesting the importance of detuning.

In fact, the differences in the spectral transitions and the appearance of hysteresis can be understood by taking into account associated shifts of the absorption peak. The molecular desorption causes a blueshift not only for E_{11} but also for the E_{22} resonance [25, 49]. Depending on the detuning, such a blueshift can result in a reduction or an enhancement of the absorption efficiency.

When we excite the nanotube near the absorption peak with $\Delta E_{\mathrm{ex}} = -3$ meV, molecular desorption shifts the peak away from the excitation energy. The efficiency of the laser-induced heating is then reduced, which suppresses further desorption of molecules. This negative feedback on molecular desorption stabilizes the amount of adsorbed molecules, and increasing the excitation power results in a smooth blueshift of the PL spectrum. As there is a one-to-one correspondence between the excitation power and the emission energy, hysteresis is absent.

In comparison, exciting at the higher energy tail of the E_{22} resonance with $\Delta E_{\mathrm{ex}} = +28$ meV leads to a positive feedback. Once the molecular desorption starts due to laser-induced heating, E_{22} moves closer to the excitation energy by the blueshift. The improved heating efficiency drives additional molecular desorption, which in turn causes a further blueshift of the E_{22} resonance. Because of this positive feedback on molecular desorption, the nanotube transitions from the cold adsorbed state with low heating efficiency to the hot desorbed state with high heating efficiency, which appears as a discontinuous blueshift at the threshold power. Considerable broadening of the desorbed state is consistent with this picture (Figure 4.3e), since the tube temperature is known to be proportional to the width of the emission peak [87–89] (see Appendix B).

The large difference in the heating efficiency for the cold adsorbed state and the hot desorbed state gives rise to the optical hysteresis (see Appendix C). For the up sweep taken with $\Delta E_{\mathrm{ex}} = +28$ meV (Figure 4.3d), $P \sim 600$ μW is required for the cold desorbed state to reach the transition temperature because of the low heating efficiency. When we sweep the excitation power down, the

nanotube stays in the hot desorbed state which has a higher heating efficiency, resulting in a transition at a much lower power of ∼400 μW compared to the up sweep.

We further investigate optical bistability at larger detuning energies. The PL excitation spectrum (Figure 4.4a) shows that the high energy tail of the E_{22} peak is steep, and thus the transition will occur at a significantly larger power when the detuning energy is increased by just tens of meV. In Figure 4.4b, the transition powers for the adsorbed and desorbed states obtained from the up and down sweeps, respectively, are plotted as a function of the detuning energy. The transition power of the adsorbed state shows a rapid increase as we expect, while the desorbed state shows a gradual increase. Such a difference can be explained by the broader absorption peak of the hot desorbed state compared to the cold adsorbed state, as the laser absorption efficiency would be less sensitive to the excitation energy. The discrepancy in the detuning energy dependence results in an increase of the width of the hysteresis, or equivalently the bistable power region, for larger ΔE_{ex}.

4.2.4 Excitation energy and polarization bistability

The results shown in Figure 4.4b suggest that the bistability can also be observed when the PL emission energies are measured as a function of detuning energy. Red filled circles in Figure 4.5a shows the excitation energy dependence taken at $P = 500$ μW for a (9,8) nanotube. When the excitation energy is swept in a direction approaching E_{22} from higher energy, a discontinuous blueshift of the emission energy occurs at $\Delta E_{\mathrm{ex}} \sim +25$ meV. When the excitation energy is swept in the opposite direction, as expected, we observe an abrupt redshift at a higher transition energy of $\Delta E_{\mathrm{ex}} \sim +35$ meV. It is also noteworthy that the emission energy shows a gradual shift when $\Delta E_{\mathrm{ex}} \lesssim 0$ meV, because the negative feedback for molecular desorption occurs at sufficiently small or negative detuning energies. When the power is lowered to 250 μW (black open circles in Figure 4.5a), the emission energy transitions are not observed anymore as the tube temperature does not reach the threshold.

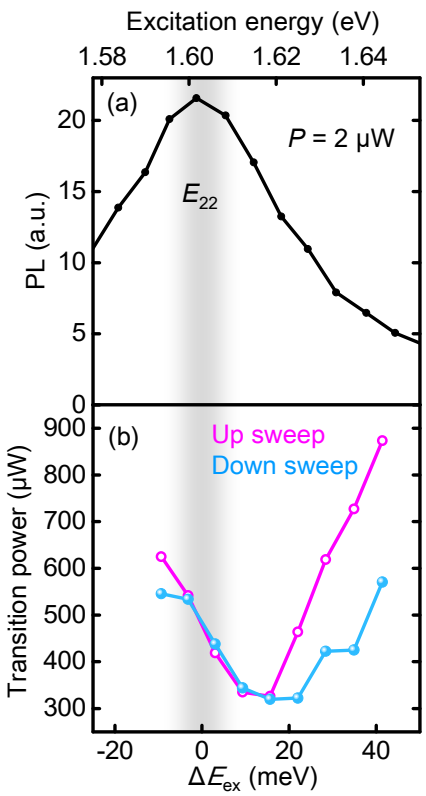

Figure 4.4: (a) PL excitation spectrum. Lorentzian fits are performed on the emission spectra in Figure 4.2a, and the peak area is plotted as a function of excitation energy. (b) Detuning energy dependence of the transition power for up sweeps (pink open circles) and down sweeps (light-blue filled circles). The transition powers are determined by interpolating the excitation power at an emission energy of 1.035 eV. The gray shaded bar indicates the E_{22} resonance determined by fitting the PL excitation spectrum in (a) with a Lorentzian function. Original data presented in Ref. [84].

In addition to the excitation energy and power dependence, the one-dimensional structure of CNTs gives rise to bistability in polarization angle dependence measurements. The absorption of an excitation beam perpendicularly polarized to the tube axis is strongly suppressed due to the depolarization effect [80], and therefore the beam polarized along the tube axis is predominantly absorbed. When we let the laser polarization angle from the tube axis to be θ, the absorbed power can be approximated by $P\cos^2\theta$. The polarization dependence should then be similar to the power dependence in Figure 4.3d. Indeed, a large optical hysteresis is observed for an excitation with $\Delta E_{\mathrm{ex}} = +34$ meV (red filled circles in Figure 4.5b), but not for a smaller detuning $\Delta E_{\mathrm{ex}} = +4$ meV (black open circles in

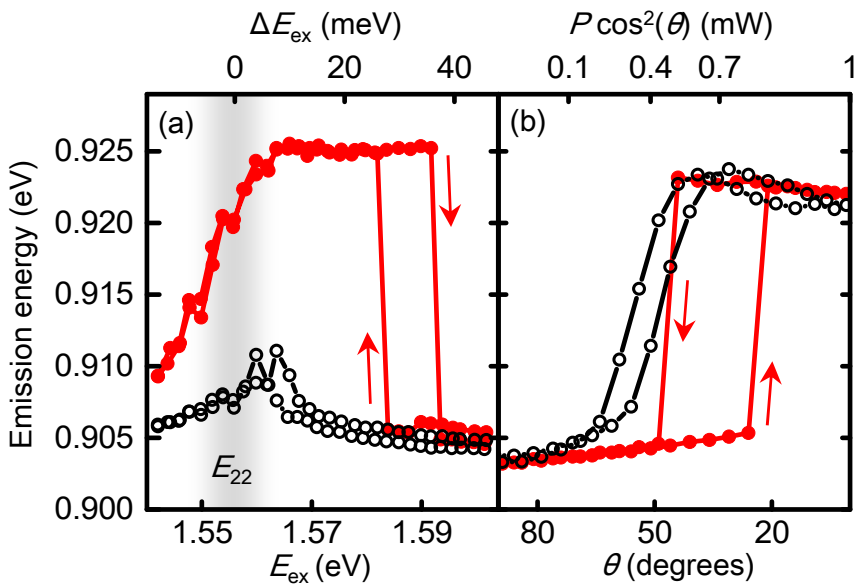

Figure 4.5: Bistability observed in excitation energy and polarization dependence for a (9,8) tube with a length of 2.01 μm. (a) Excitation energy dependence of the emission energy measured with $P = 500$ μW (red filled circles) and 250 μW (black open circles), taken with polarization parallel to the tube axis. The gray shaded bar indicates the E_{22} resonance for this nanotube determined from a PL excitation spectrum taken with the same polarization at $P = 5$ μW. (b) Polarization dependence of the emission energy measured with $\Delta E_{\text{ex}} = +34$ meV (red filled circles) and +4 meV (black open circles), taken at $P = 1.00$ mW. For both panels, the emission energies are determined by fitting the spectra with a Lorentzian function. Original data presented in Ref. [84].

Figure 4.5b).

4.3 All-optical memory operation

4.3.1 Principle of memory operation

The optical hysteresis loops can be exploited to achieve memory operation, since the two stable emission states reflect their excitation history (Figure 4.6). During an up-sweep power dependence measurement, the nanotube stays in the adsorbed state as long as the power is within the bistable region. Switching to the desorbed state occurs at the transition power, and the nanotube remains in this state during a down sweep until the power is reduced below the bistable region. It should be possible to sustain the emission state by exciting at the power within the bistable region, whereas appropriate modulation of the excitation power would allow for

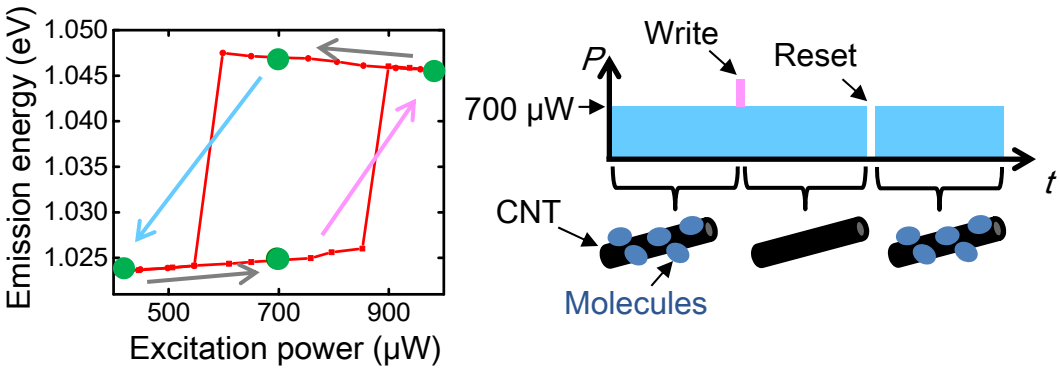

Figure 4.6: Schematic of the memory operation. Original data presented in Ref. [84].

switching between the states.

4.3.2 Optical setup

To verify whether CNTs can actually operate as a rewritable optical memory, we have constructed an optical system that can generate an excitation pattern shown in Figure 4.6 and simultaneously detect PL signal from nanotubes (Figure 4.7). In this system, a polarizing beam splitter is used for separating the laser beam into two orthogonal polarizations, and the ratio of the two beams is controlled by rotating the polarization before the beam splitter. The transmitted beam is used for the bias beam, and the reflected beam is used for the set pulses by placing a shutter in its path. We use another shutter before the beam splitter to perform reset operations. The two beams are directed towards the objective lens using a second polarizing beam splitter, and we rotate the polarization of the beams to be $\theta = \pm 45°$ with a half-wave plate placed after this beam splitter. We note that the power absorbed by the nanotubes is therefore half of the power P measured at the sample.

4.3.3 Reversible and reproducible optical memory operation

We measure the temporal changes of PL for a different (9,8) nanotube using this system. The temporal evolutions of the spectrally integrated PL for the energies of adsorbed and desorbed states are shown in Figure 4.8b, and the corresponding

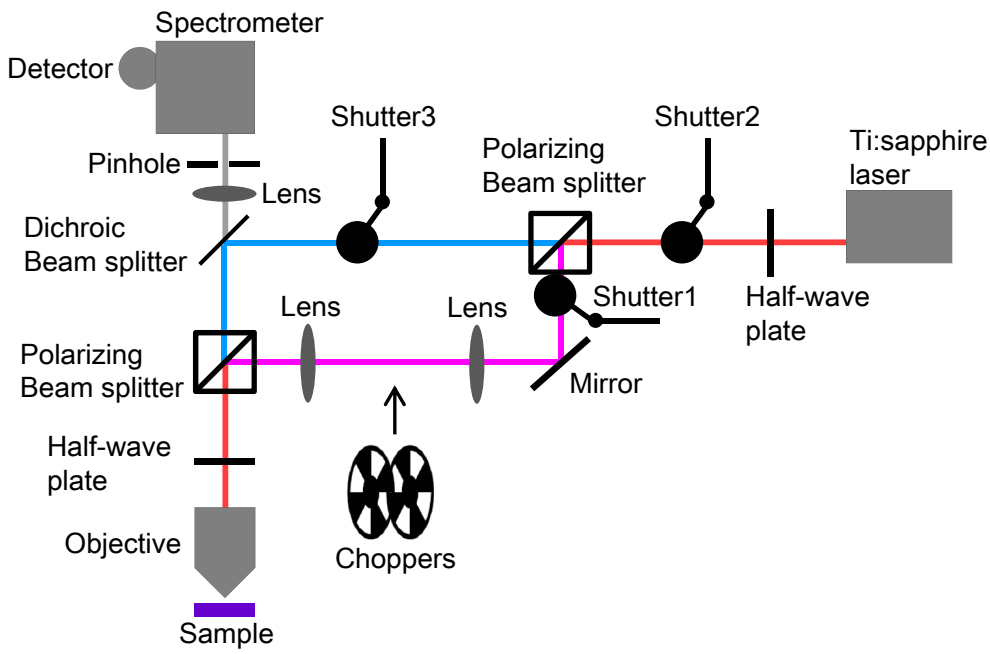

Figure 4.7: Measurement setup for time-domain measurements. In the demonstration of the single CNT optical memory, Shutter 1 and Shutter 2 are used for the set and reset operations, respectively. In the time-resolved measurements, optical choppers are installed at the focus of the lens pair to obtain the optical pulses. Shutter 3 is used for taking the PL spectrum without the probe beam. An original schematic presented in Ref. [84].

emission spectra are shown in Figure 4.9

In this measurement, the power of the bias beam is tuned to the center of the bistable power region of the nanotube, while the power of the set pulse is adjusted so that it can induce a transition. At the start of the measurement, a shutter is opened to begin exciting the nanotube with the bias beam. The low-energy PL intensity (red line in Figure 4.8b) is large while the high-energy PL intensity (blue open circles in Figure 4.8b) is small, indicating that the nanotube is initially in the adsorbed state. One minute after the start of the measurement, a set pulse is added to the bias beam by opening another shutter for a less than a second. The set pulse increases the temperature of the nanotube and switches its state from the adsorbed state to the desorbed state. The switching behavior can be seen as an abrupt increase of the high-energy PL intensity as well as a decrease of the low-energy PL intensity. After another minute from the set operation, the bias beam is blocked by the shutter to perform the reset operation. The

nanotube switches back to the adsorbed state and the low-energy PL intensity recovers. We note that the nanotube maintains its emission state during the one-minute intervals between the set and reset operations, showing that the width of the bistable power region is sufficiently large compared to the fluctuations of the absorbed laser power. The results of this measurement confirm the rewritability and the stability of the single CNT optical memory.

We further repeated the switching cycles to check the reliability of the memory operation. In Figure 4.8c, we plot the temporal evolution for the low-energy PL intensity. Reversible and reproducible switching operations of over 45 times are demonstrated, suggesting that the nanotube optical memory can also be manipulated under a more complicated sequence of light pulses.

4.4 Time-resolved measurements

Rewriting speed is an important factor in the performance of optical memories. In the case of our nanotube optical memory, the time scale should be limited by the molecular desorption or adsorption times.

4.4.1 Optical pulse generation utilizing optical chopper

Here we utilize chopper controlled optical pulses to elucidate the time scales. In desorption-time measurements, we have stacked two chopper wheels to achieve a duty cycle of 0.0053. Even for the highest frequency used in our measurements, the pulse interval is longer than 16 ms due to the low duty cycle, which is still long enough for re-adsorption of the molecules. In the adsorption-time measurements, two optical choppers are synchronized to the same reference. The frequency and the phase difference are controlled to vary t_{i} while keeping $t_{\mathrm{w}} = 0.4$ ms. In both cases, choppers are located the middle of the lens pair (Figure 4.7).

4.4.2 Desorption times

We start with the investigation of the molecular desorption times by measuring the changes of the PL spectra as a function of the excitation pulse width t_{w}

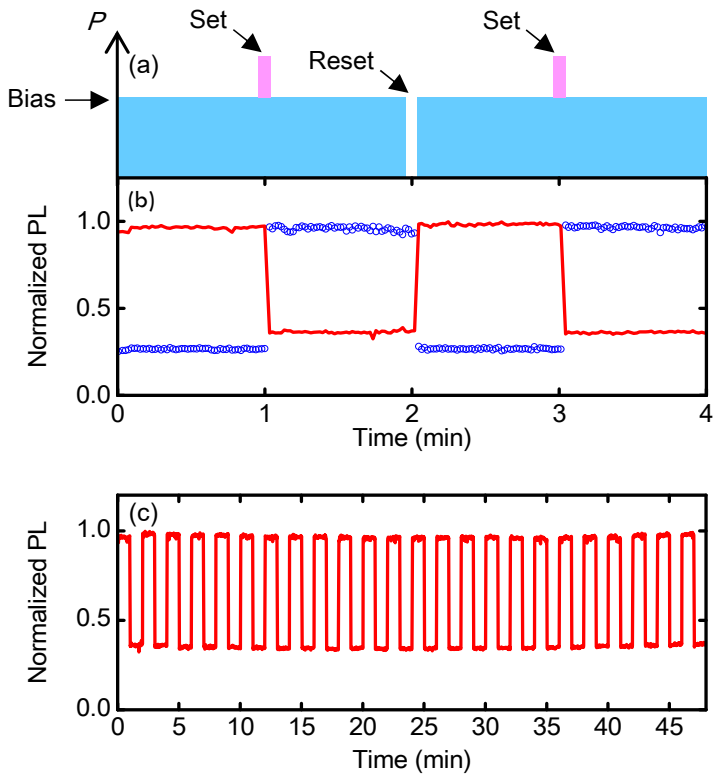

Figure 4.8: Reversible and reproducible memory operation of a 2.00-μm-long (9,8) tube. (a) Schematic showing the temporal pattern of excitation power. (b) Temporal evolution of integrated PL intensities for emission energies of 0.904 eV (red line) and 0.921 eV (blue open circles). The spectral integration windows are 4 meV wide, and the intensities are normalized by the maximum values. In this measurement, the detuning energy is +42 meV. The bias beam is tuned to be $P = 1.70$ mW and $\theta = -45°$, and the set pulses are set to $P = 0.89$ mW and $\theta = +45°$. (c) Further evolution of integrated PL at 0.904 eV obtained by continuing the measurement in (b). Original data presented in Ref. [84].

(Figure 4.10a), using a power high enough to desorb the molecules. The measurements have been performed on another (9,8) tube, and two representative time-integrated PL spectra are shown in Figure 4.10b. The spectrum taken with $t_{\mathrm{w}} = 1.3$ ms shows a large contribution from the blueshifted desorbed-state peak at 0.921 eV, which is reasonable because all molecules should have desorbed for sufficiently long t_{w}. In the case of the spectrum taken with $t_{\mathrm{w}} = 0.084$ ms, however, the adsorbed-state peak at 0.906 eV is pronounced. The single peak at a lower-energy shows that most of the molecules stay adsorbed during the pulse, indicating that t_{w} is much shorter than the desorption time.

In order to extract the desorption time τ_{d}, we analyze the time-integrated PL

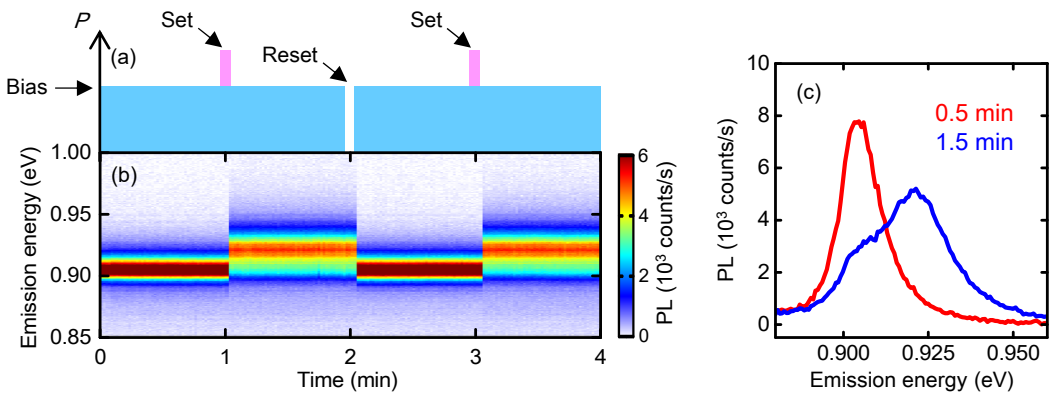

Figure 4.9: (a) Schematic showing the temporal pattern of excitation power. (b) Temporal evolution of the emission spectra for the data shown in Figure 4.8. (c) Emission spectra at 0.5 min (red curve) and 1.5 min (blue curve). For this tube, we observe some residual low-energy component for the desorbed state. Original data presented in Ref. [84].

spectra taken for various pulse widths. Bi-Lorentzian fits to the spectra are performed to obtain the desorbed-state and adsorbed-state peak areas (Figure 4.11). We then numerically differentiate the peak area by t_{w} to examine the transient behavior of the nanotube during the excitation pulse (Figure 4.10c). The intensity of PL from the desorbed state (blue crosses) increases as the pulse width becomes wider, while the intensity of PL from the adsorbed state (red open circles) decreases. Both intensities reach constant values at longer pulse widths, showing that all molecules have desorbed. We fit the transient PL intensities of the desorbed state and the adsorbed state with $I_{\mathrm{PL}} = I_0[1 - \exp(-(t_{\mathrm{w}} - t_0)/\tau_{\mathrm{d}})]$ and $I_{\mathrm{PL}} = I_1 \exp(-(t_{\mathrm{w}} - t_0)/\tau_{\mathrm{d}})$, respectively, where I_0 is the saturation intensity, I_1 is the initial intensity, and t_0 is the offset time. Solid curves in Figure 4.10c are the best fits to the data, where we obtain comparable values of $\tau_{\mathrm{d}} = 0.15$ ms (blue curve) and 0.13 ms (red curve).

The desorption times are known to become shorter for higher material temperatures [90], and therefore we expect τ_{d} to decrease for larger excitation powers. We have taken the t_{w} dependence of the spectra at various powers and the results are summarized in Figure 4.10d. Indeed, τ_{d} becomes shorter as the power increases, indicating that the molecules do desorb faster.

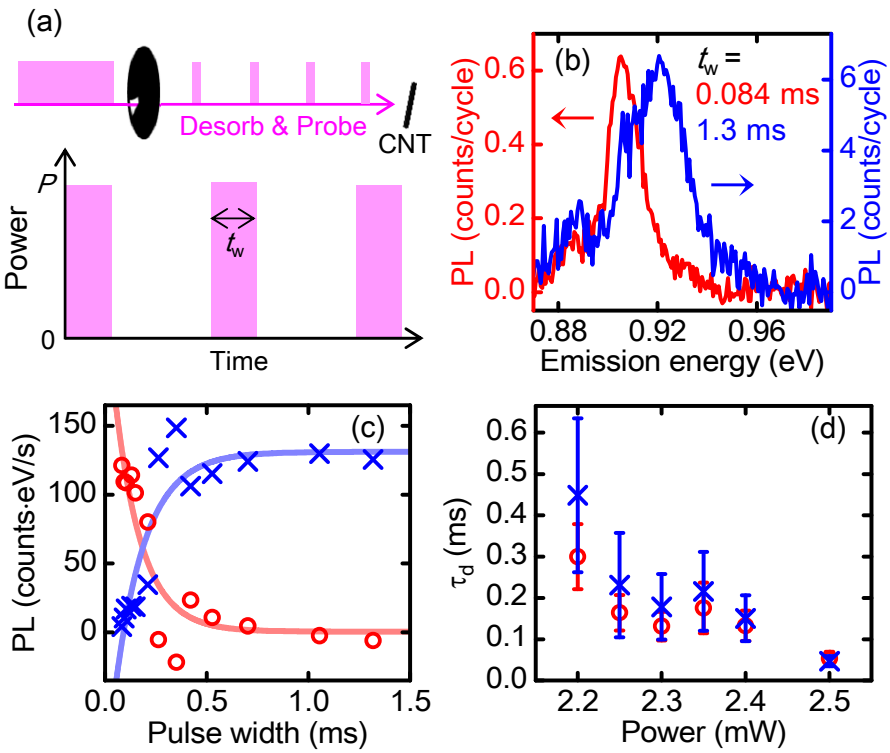

Figure 4.10: Desorption time measurements. (a) Schematic of the measurements showing an excitation pulse pattern and the definition of t_w. (b) Time-integrated PL spectra taken with $t_w = 0.084$ ms (red curve, left axis) and 1.3 ms (blue curve, right axis). (c) Transient PL intensities of the high-energy peak (blue crosses) and the low-energy peak (red open circles). Blue and red curves are fits as explained in the text. (d) Pulse power dependence of τ_d. The transient PL intensities of the high-energy peak and the low-energy peak are used to obtain the blue crosses and the red open circles, respectively. (b-d) are taken with $\Delta E_{ex} = +40$ meV and $\theta = +45°$ on a 2.62-μm-long (9,8) tube, and (b,c) are measured at $P = 2.40$ mW. Original data presented in Ref. [84].

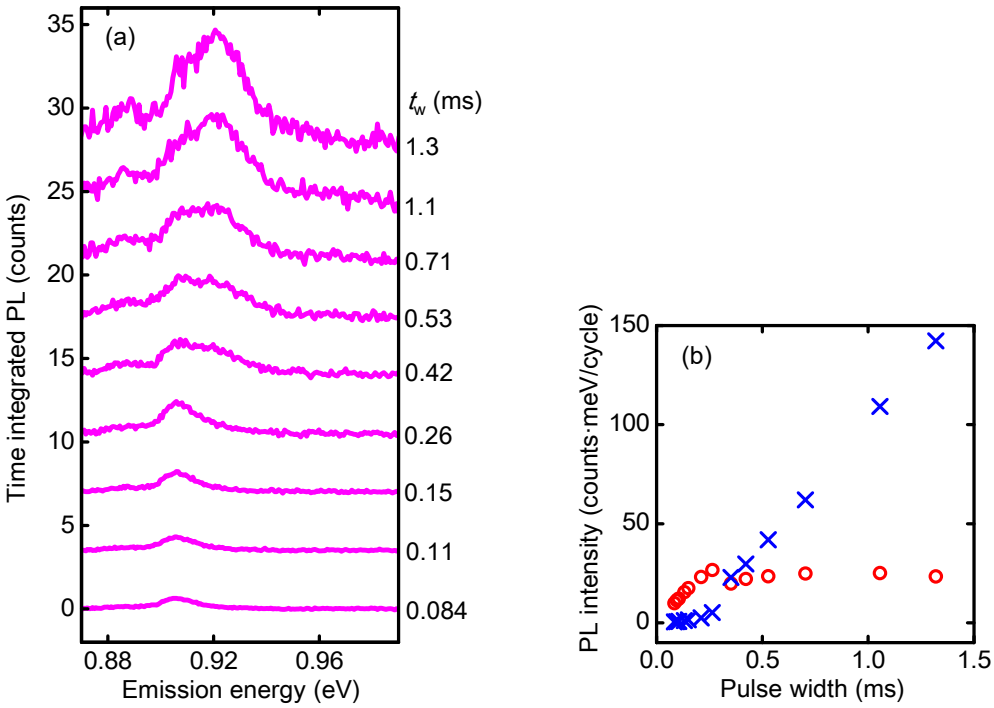

Figure 4.11: (a) t_w dependence of the time-integrated PL spectra. (b) tw dependence of the time-integrated PL intensities of the high-energy peak (blue crosses) and the low-energy peak (red open circles). Figure 4.10c is obtained by numerically differentiating the data in (b) by t_w. Original data presented in Ref. [84].

4.4.3 Adsorption times

The measurements for molecular adsorption times are not as straightforward as the desorption-time measurements, because adsorption occurs in between the pulses when nanotubes are not emitting. We therefore introduce a weak continuous beam for probing the amount of adsorbed molecules during the pulse interval time t_i (Figure 4.12a). The probe beam power is kept sufficiently low to minimize laser-induced heating, while the desorption pulses are set to high enough powers. As the desorption pulses inevitably cause strong PL, we take the difference between the time-integrated spectra with and without the probe beam to examine the adsorption dynamics during the pulse intervals.

Figure 4.12b shows two PL difference spectra taken at long (t_i = 7.0 ms, red curve) and short (t_i = 0.5 ms, blue curve) intervals. In these spectra, two distinct peaks at 0.906 eV and 0.933 eV are observed, which correspond to the adsorbed and desorbed states, respectively. In the spectrum taken at t_i = 7.0 ms,

the low-energy peak dominates the spectrum, showing that the molecules have already adsorbed. In comparison, the peak at the higher energy is prominent in the spectrum measured at $t_{\mathrm{i}} = 0.5$ ms, indicating that molecular adsorption is insubstantial at this short interval time.

We note that the higher energy peaks in Figure 4.12b and Figure 4.10b are located at slightly different energies, although both peaks should correspond to the desorbed state. Such a difference is reasonable, as the nanotube is probed with significantly higher powers in the desorption-time measurements compared to the adsorption-time measurements. Since the temperature of the nanotube should be higher, heating-induced redshift is expected [87]. In comparison, the lower-energy peaks are at the same energy in Figure 4.12b and Figure 4.10b, indicating that the heating effect is negligible for the adsorbed state.

We further examine the adsorption dynamics by analyzing the inter-pulse emission using t_{i} dependence of the PL difference spectra (Figure 4.13). As in the case for the desorption-time measurements, the emission spectra are fitted with a bi-Lorentzian function to obtain the peak areas, and we numerically differentiate the peak areas by t_{i} to evaluate the transient emission states during the pulse interval (Figure 4.12c). The PL intensity from the adsorbed state increases for longer t_{i} (red open circles), while emission from the desorbed state decreases (blue crosses).

To extract the molecular adsorption time τ_{a}, $I_{\mathrm{PL}} = I_1[1 - \exp(-(t_{\mathrm{i}} - t_0)/\tau_{\mathrm{a}})]$ and $I_{\mathrm{PL}} = I_0 \exp(-(t_{\mathrm{i}} - t_0)/\tau_{\mathrm{a}})$ are fit to the adsorbed state and the desorbed state emission intensities, respectively (see Appendix D). The best fitted curves are shown in Figure 4.12c, and similar values of $\tau_{\mathrm{a}} = 1.0$ ms (red curve) and 1.2 ms (blue curve) are obtained. The adsorption time is about an order of magnitude longer than the desorption times, limiting the rewriting speed of the nanotube optical memories.

We have also investigated the desorption-pulse power dependence of adsorption time, and the results are summarized in Figure 4.12d. We do not observe a clear power dependence for τ_{a}, although measurements up to higher powers have been performed compared to the τ_{d} measurements. The absence of power

dependence is expected, since the adsorption time only depends on the molecular collision frequency if the sample cooling time does not limit the experimental resolution [91–93]. It should be possible to shorten the adsorption time by increasing the humidity, as the collision frequency is determined by the partial pressure of the molecules.

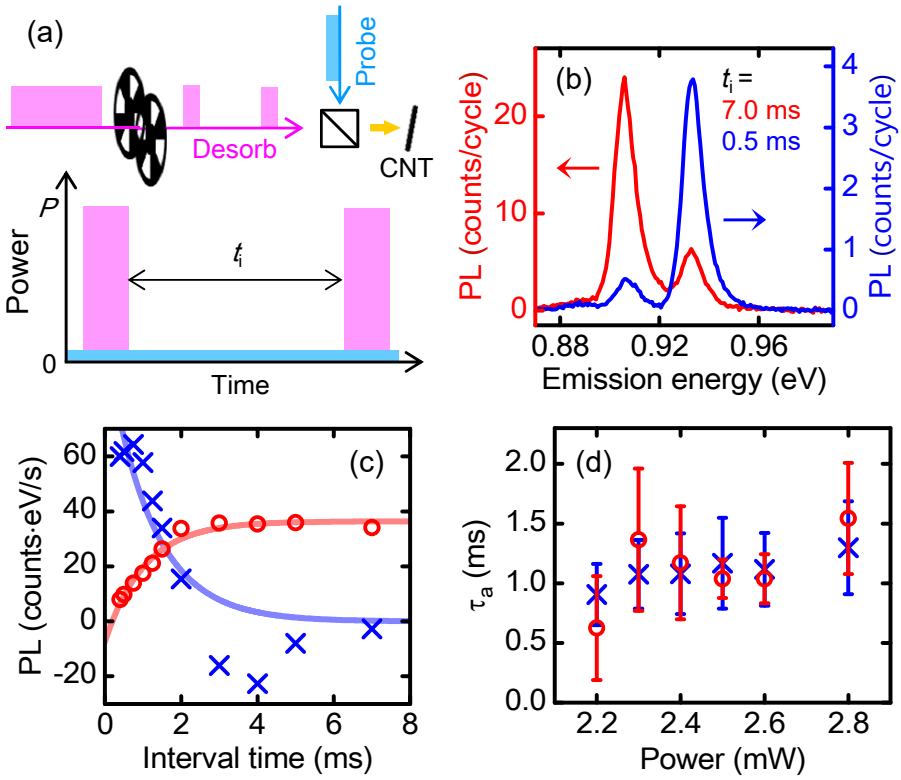

Figure 4.12: Adsorption time measurements. (a) Schematic of the measurements showing desorption pulses and a probe beam as well as the definition of t_i. (b) PL difference spectra taken with $t_i = 7.0$ ms (red curve, left axis) and 0.5 ms (blue curve, right axis). (c) Transient PL intensities of the low-energy peak (red open circles) and the high-energy peak (blue crosses). Red and blue curves are fits as explained in the text. (b,c) are measured at $P = 2.50$ mW. (d) Pulse power dependence of τ_a. The transient PL intensities of the low-energy peak and the high-energy peak are used to obtain the red open circles and the blue crosses, respectively. All data are taken with $\Delta E_{ex} = +40$ meV, and the power ratio of the desorption pulses to the probe beam is adjusted to be 1:0.017. The desorption pulses and probe beam are set to $\theta = +45°$ and $-45°$, respectively. Original data presented in Ref. [84].

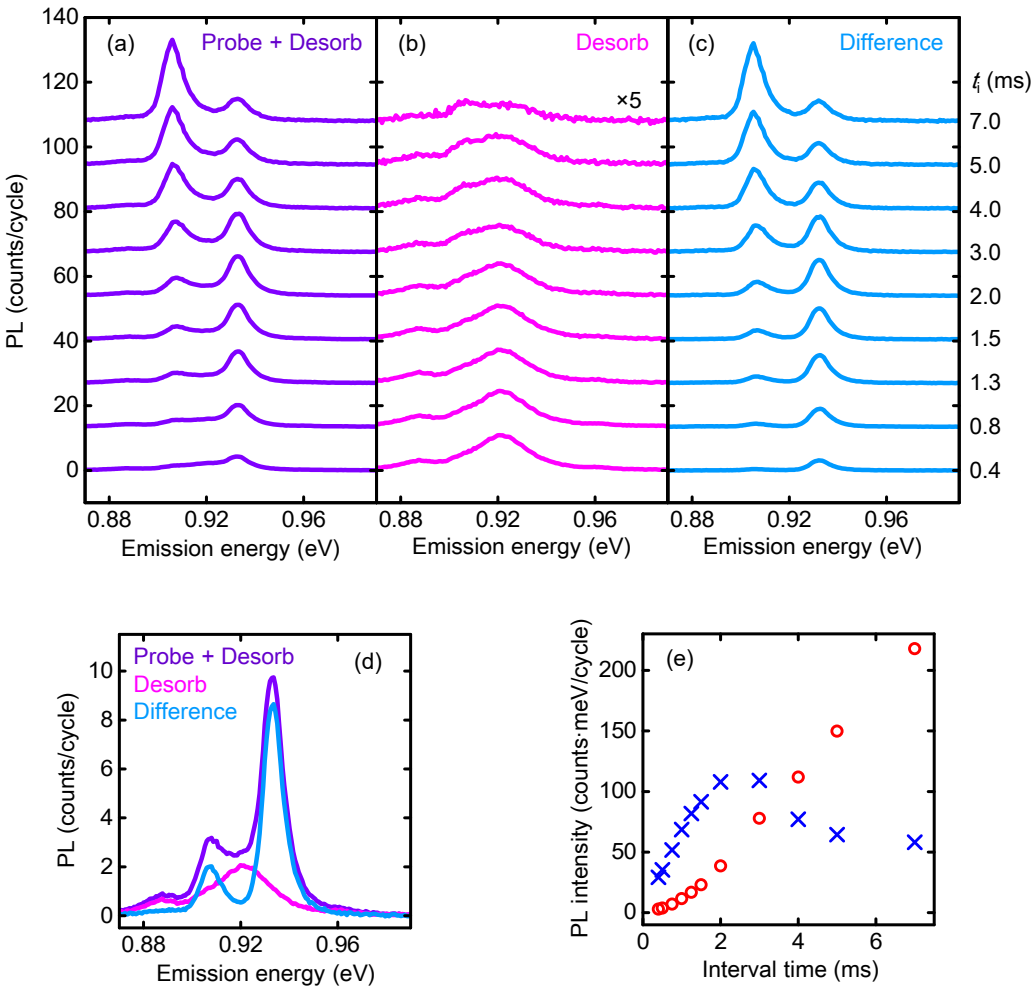

Figure 4.13: t_i dependence of the time-integrated PL spectra taken with (a) both the probe beam and the desorption pulses and (b) only with the desorption pulse. PL intensities shown in (b) are expanded 5 times. (c) Difference of (a) and (b). (d) PL spectra at t_i = 1.3 ms from data in (a) (purple curve), (b) (pink curve), and (c) (cyan curve). (e) tw dependence of time-integrated PL intensities of the high-energy peak (blue crosses) and the low-energy peak (red open circles). Figure 4.12c is obtained by numerically differentiating the data in (e) by t_i. Original data presented in Ref. [84].

4.5 Summary

We observe optical bistability in individual CNTs, where switching between the hot desorbed state and the cold adsorbed state is triggered by a change in the excitation laser power. A direct readout of the nanotube state is possible, as the emission energy switches simultaneously. The E_{22} resonance shift associated with molecular adsorption causes a considerable difference in the laser heating efficiency, locking the nanotube into either of the two states. Furthermore, we demonstrate reversible and reproducible optical memory operation, and obtain the adsorption and desorption times by performing time-resolved measurements.

Our results highlight the potential use of CNTs for ultrasmall optical memories and switches in photonic circuits, surpassing the size limits imposed by the cavities. Taking advantage of various chiralities and polarization selectivity, it should be possible to address individual nanotubes even if they are located in the vicinity. The functionality of the nanotube optical memory is provided by the few molecules on the surface, which is coupled to the characteristic absorption peak through the strong effects of screening. Being telecom-band emitters that can be integrated with silicon photonics, CNTs present opportunities for optical devices with operation mechanisms at the molecular level.

Chapter 5

Conclusions

We have elucidated the screening effects on excitons in individual air-suspended carbon nanotubes, and explored the potential applications utilizing its exceptional properties.

By performing simultaneous PC and PL excitation spectroscopy, various excitonic states under bias voltages have been investigated. As the applied bias field is increased, we observe an emergence of new absorption peaks in the excitation spectra. Measurements on various nanotubes with different chirality show that there is a clear diameter dependence on the energy separation between the bias-induced peaks and the emission energies. From the diameter dependence, we attribute the peaks to the dark excited excitonic states which become optically active due to electrically-induced symmetrical breaking. The observed $2g$ state is compared with the results of previous two-photon measurements on micelle tubes, and the comparison show that the environmental screening changes the excitonic energies by more than a factor of 2. Furthermore, we have obtained exceptionally large exciton binding of 620 meV by subtracting the PL emission energy from the E_{11} continuum edge. These results highlight the importance of surrounding screening medium on optical properties of carbon nanotubes.

We exploit such exceptional screening effects on excitons for controlling the optical properties of single carbon nanotubes in optical means. Power dependence measurements with various detuning energies show that the tubes can switch between the hot desorbed state and the cold adsorbed state, and the switching

behaviors are abrupt when the excitation energies are sufficiently higher than the E_{22} peak. At such large detuning, we have also observed optical bistability. Changes of laser heating efficiency due to the shift of E_{22} peak explain the observed hysteresis, and the corresponding emission linewidth supports our interpretation. The optical bistability is also observed in excitation energy and polarization measurement, showing flexibility of our optical manipulation technique utilizing molecular screening effects.

To show that the optical hysteresis loops lead to achieve memory functionality, we have constructed the system where the excitation laser beams are separated into two paths and the computer controlled shutters block the beams at arbitrary timing. By using this system, we have demonstrated reversible and reproducible switching operation of 1 minute cycles for more than 45 times. The switching speed, which correspond to the molecular adsorption and desorption times, are also elucidated by time-resolved measurements utilizing choppers.

Our results underscore the impact of screening effects on electrical bandgap and excitonic energies in carbon nanotubes. In principle, such effects would also cause a large modification on the transport properties, and should also be applicable to other low-dimensional materials as the modification is occurred through local dielectric screening. We hope that our findings will lead to new design strategies towards light emitters, detectors, transistors, and memories at the nanoscale.

Appendix A

Nitrogen purging system

In order to prevent oxygen-induced defect formation, we have constructed a system where the sample space is purged with nitrogen. In Figure A.1a, we show a schematic of the system. We directly take dry nitrogen gas from a vent valve of a nitrogen tank, and the gas is guided to the sample by plastic tubes. The gas is purged into the sealed space between the stage and the objective lens holder. The flow rate is controlled to be 1.0 ℓ/min by a flowmeter. A photograph the objective is also shown in Figure A.1b, where we have removed the automated stage to make it clear to see.

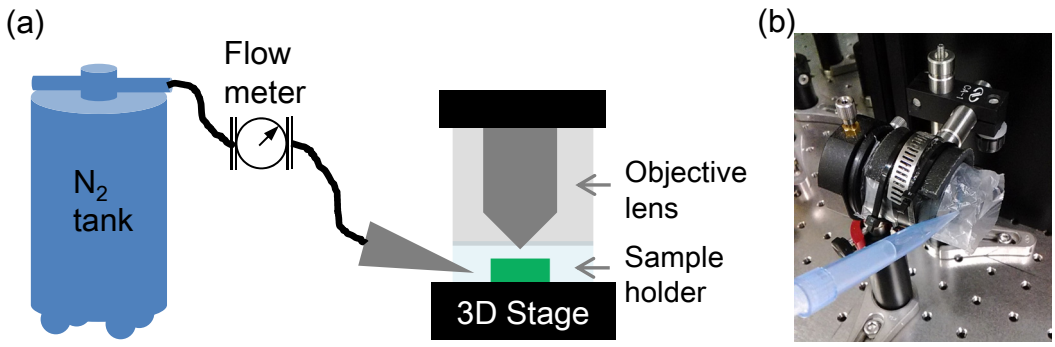

Figure A.1: (a) A schematic of a nitrogen purging system. (b) A picture around the sample.

Appendix B

Estimation of the nanotube temperature

Let us discuss the tube temperature quantitatively. We estimate the temperature for a nanotube in a desorbed state as the tube is no longer influenced by molecules. We assume that the temperature is linearly depended on the full-width at half-maximum Γ, which is previously observed in temperature dependent measurements [87–89]. If the cause of the broadening is dominated by the laser heating, and if the temperature shows a linear dependence on the excitation power, the tube temperature T^* can be estimated from

$$\Gamma = \Gamma_0 + \alpha T^* = \Gamma_0 + \alpha(\gamma P + 300), \tag{B.1}$$

where $\alpha = 0.025$ (meV/K) is the heating coefficient [87], Γ_0 is the residual linewidth, and γ is the laser heating coefficient. We have assumed that the tube temperature is 300 K at $P = 0$ μW. By fitting the result in Figure B.1, we obtain $\gamma = 0.45$ K/μm and $\Gamma_0 = 3.3$ meV for this nanotube. The estimation seems somehow overestimating the temperature, because the relation suggest that the molecular desorption occurs at $T^* \sim 500$ K ($P = 450$ μW), while the previous temperature-dependent measurement on similar diameter nanotube under the same ambient show molecular desorption at 330 K for [46].

The corresponding redshifts also suggest that the estimation is overestimating. Since an increase of the temperature cause emission energy shifts, we estimate

the magnitude by using the empirical Varshni functional form

$$\Delta E = -\frac{\alpha T^2}{\beta + T^*}, \tag{B.2}$$

where $\alpha = 0.075$ meV/K and $\beta = 600$ K [87]. We calculate the shift from the initial data point in Figure B.1 using Equation B.1. The result indicate that a much larger redshift should occur if the tube temperature is correctly estimated. The actual tube temperature might be lower than our estimation.

There might be the other processes causing the broadening, such as photocarrier and exciton-exciton annihilation effects. The other possibility is that the exciton temperature and the lattice temperature are not the same. Further investigation is required to clarify the underlying physics.

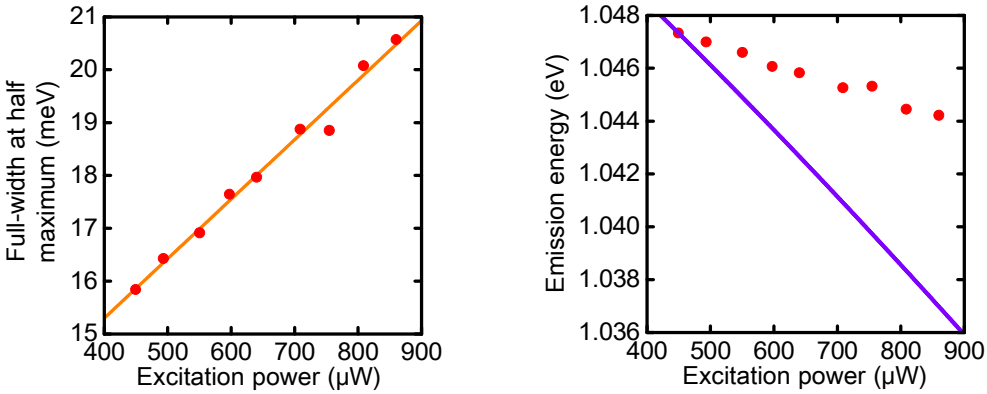

Figure B.1: (a) Excitation power dependence of full-width at half-maximum. (b) Excitation power dependence of emission energy. (a,b) are the same with the down sweep data taken with $\Delta E_{\mathrm{ex}} = +28$ meV in Figure 4.3. The red dots are the data, the orange line is the fit, and the purple line is the estimated shifts. Original data presented in Ref. [84].

Appendix C

Additional discussion on the optical bistability

In order to understand the observed bistable behavior in more detail, here we construct a simple model that can explain the experimental results.

As the molecular desorption causes blue shifts in the excitonic resonances [25, 49], absorption efficiency would be increased when we excite the tube at a higher energy tail of the E_{22} resonance (Figure C.1). For the red detuning case, however, the efficiency should decrease through the desorption process.

Such changes occur when the tube temperature exceeds the threshold where

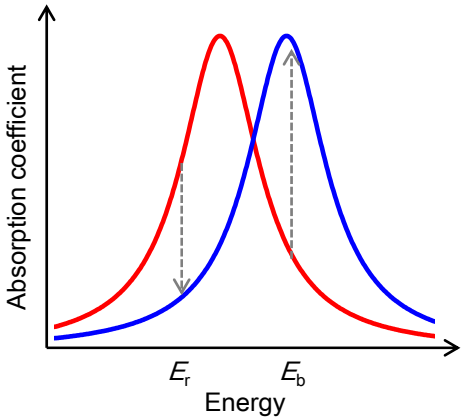

Figure C.1: A schematic of absorption spectra for a nanotube in adsorption (red curve) and desorption (blue curve) states. The energy E_r and E_b denote the case with red and blue detuning excitation, respectively. The dashed lines show the changes of absorption efficiencies at each excitation energy.

molecular desorption takes place [46,49]. The relationship between the absorption efficiency α and tube temperature ΔT can therefore be roughly expressed by the following equation

$$\alpha = \begin{cases} \alpha_{\mathrm{a}} & (\Delta T < T_1) \\ \frac{\alpha_{\mathrm{d}} - \alpha_{\mathrm{a}}}{T_2 - T_1}(\Delta T - T_1) + \alpha_{\mathrm{a}} & (T_1 \leq \Delta T \leq T_2) \\ \alpha_{\mathrm{d}} & (\Delta T > T_2), \end{cases} \tag{C.1}$$

where we let α_{a} and α_{d} be absorption coefficients of nanotubes in the adsorption and desorption states, respectively, and we let T_i $(i = 1, 2)$ be the transition temperatures. Difference from room temperature is used as ΔT for simplicity.

In the case of laser heating, the increase of the tube temperature induced by excitation power P should have a relation

$$\alpha = \frac{1}{\kappa P}\Delta T, \tag{C.2}$$

where κ denotes the heating coefficient.

It is clear from Figure C.2ab that Equation C.1 and Equation C.2 can have multiple solutions in the case of blue detuning, but only a solution for the red detuning. For an easier comparison with the experimental data, we plot the ΔT as a function of P in Figure C.2cd. We now obtain a result similar to that presented in Figure 4.3e, showing that the laser-heating induced molacular desorption can give rise to the observed optical bistability.

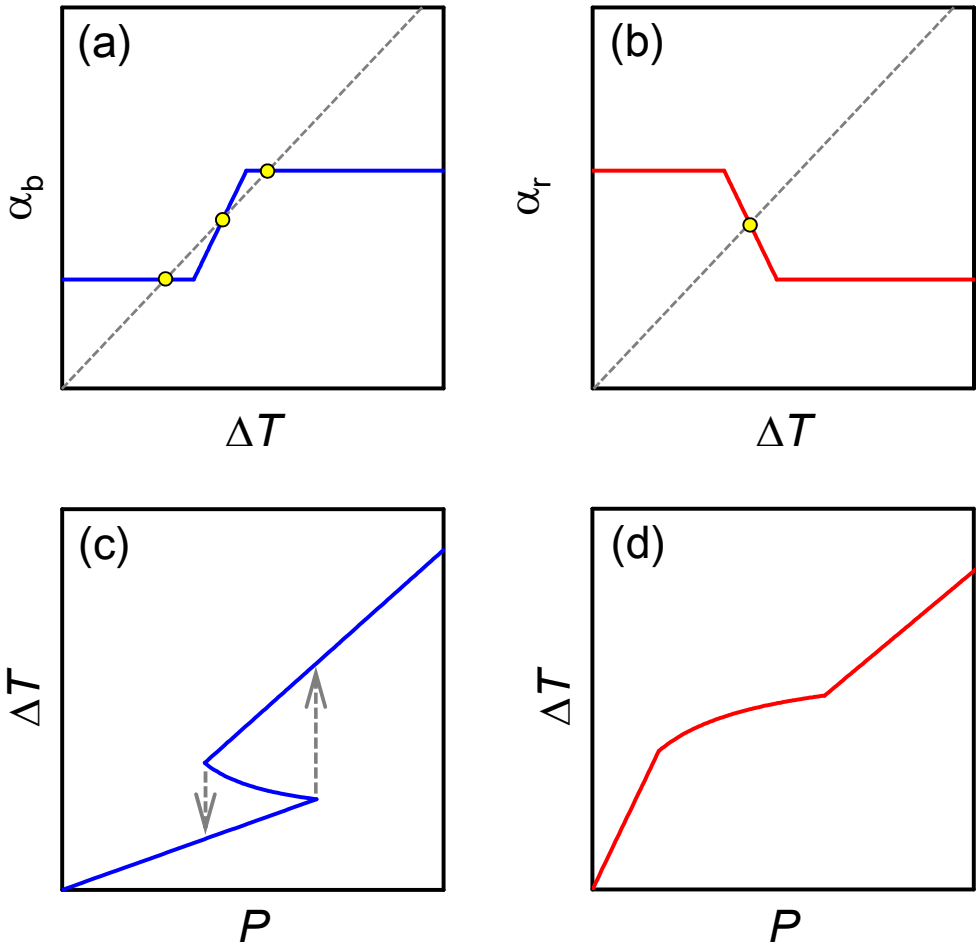

Figure C.2: (a) and (b) The blue and red curves are indicating Equation C.1 for the blue and red detuning case, respectively. The dashed gray line denotes Equation C.2 and the yellow circles indicate the intersections. (c) and (d) are showing the solutions of (a) and (b), respectively.

Appendix D

Additional discussion on the adsorption time

We observe negative intensities in the transient PL of the high-energy peak at around 4 ms (Figure 4.12c), which is not expected for the simple model discussed in the main text. Negative values of the numerical derivative correspond to decreasing time-integrated PL intensities (Figure 4.13e). The non-monotonic behavior can be explained by assuming that the adsorption time has t_{i} dependence, which can happen if the amount of molecules responsible for re-adsorption changes with the interval time. Desorption should mostly occur within the laser spot, but molecules outside of the excitation region maybe desorbing at short interval times. As less molecules can be adsorbed during the pulse intervals, the energy from the laser excitation may be able to desorb molecules outside the laser spot, increasing the adsorption time. In order to take into account the t_{i} dependence, we let the adsorption time to be

$$\tau_{\mathrm{a}}(t_{\mathrm{i}}) = (\tau_{\mathrm{a}}^{0} - \tau_{\mathrm{a}}^{1}) \exp(-\frac{t_{\mathrm{i}}}{t_{\mathrm{tr}}}) + \tau_{\mathrm{a}}^{1}, \tag{D.1}$$

where τ_{a}^{0} is initial adsorption time, τ_{a}^{1} is the final adsorption time, and t_{tr} is the transition time. The time-integrated PL of the desorbed state and the adsorbed state are given by

$$\begin{aligned} U(t_{\mathrm{i}}) &= \int_{0}^{t_{\mathrm{i}}} I_{1} \exp(-\frac{t}{\tau_{\mathrm{a}}(t_{\mathrm{i}})}) dt \\ &= I_{1} \tau_{\mathrm{a}}(t_{\mathrm{i}}) [1 - \exp(-\frac{t_{\mathrm{i}}}{\tau_{\mathrm{a}}(t_{\mathrm{i}})})], \end{aligned} \tag{D.2}$$

and

$$
\begin{aligned}
U(t_{\mathrm{i}}) = & \int_0^{t_{\mathrm{i}}} I_0[1-\exp(-\frac{t}{\tau_{\mathrm{a}}(t_{\mathrm{i}})})]dt \\
= & I_0[t_{\mathrm{i}} + \tau_{\mathrm{a}}(t_{\mathrm{i}})\exp(-\frac{t_{\mathrm{i}}}{\tau_{\mathrm{a}}(t_{\mathrm{i}})}) - \tau_{\mathrm{a}}(t_{\mathrm{i}})],
\end{aligned}
\tag{D.3}
$$

respectively. These equations can reproduce the data if we assume $t_{\mathrm{tr}} = 3$ ms (Figure D.1a,b). We also plot the interval-time dependence of the adsorption time according to this model (Figure D.1c).

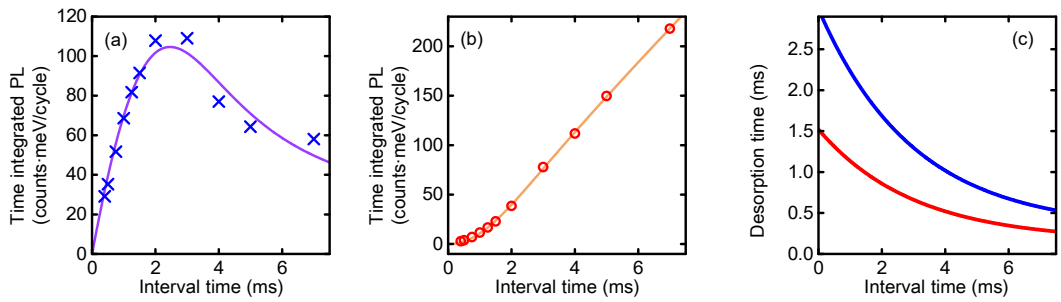

Figure D.1: (a) and (b) Interval-time dependence of the time-integrated PL intensities of the high-energy peak [blue crosses in (a)] and the low-energy peak [red open circles in (b)]. Curves in (a) and (b) are fits using Equation D.2 and Equation D.3, respectively. (c) Interval-time dependence of the adsorption time obtained from the data in (a) (blue curve) and (b) (red curve). Original data presented in Ref. [84].

References

[1] S. Iijima, T. Ichihashi, *Nature* **363**, 603 (1993).

[2] T. Ando, *J. Phys. Soc. Jpn.* **66**, 1066 (1997).

[3] N. Hamada, S.-i. Sawada, A. Oshiyama, *Phys. Rev. Lett.* **68**, 1579 (1992).

[4] M. Bockrath, D. H. Cobden, P. L. McEuen, N. G. Chopra, A. Zettl, A. Thess, R. E. Smalley, *Science* **275**, 1922 (1997).

[5] J. A. Misewich, R. Martel, P. Avouris, J. C. Tsang, S. Heinze, J. Tersoff, *Science* **300**, 783 (2003).

[6] J. Chen, V. Perebeinos, M. Freitag, J. Tsang, Q. Fu, J. Liu, P. Avouris, *Science* **310**, 1171 (2005).

[7] J. U. Lee, *Appl. Phys. Lett.* **87**, 073101 (2005).

[8] N. M. Gabor, Z. Zhong, K. Bosnick, J. Park, P. L. McEuen, *Science* **325**, 1367 (2009).

[9] N. Higashide, M. Yoshida, T. Uda, A. Ishii, Y. K. Kato, *Appl. Phys. Lett.* **110**, 191101 (2017).

[10] S. Imamura, R. Watahiki, R. Miura, T. Shimada, Y. K. Kato, *Appl. Phys. Lett.* **102**, 161102 (2013).

[11] R. Miura, S. Imamura, R. Ohta, A. Ishii, X. Liu, T. Shimada, S. Iwamoto, Y. Arakawa, Y. K. Kato, *Nat. Commun.* **5**, 5580 (2014).

[12] F. Pyatkov, V. Fütterling, S. Khasminskaya, B. S. Flavel, F. Hennrich, M. M. Kappes, R. Krupke, W. H. P. Pernice, *Nat. Photon.* **10**, 420 (2016).

[13] H. Machiya, T. Uda, A. Ishii, Y. K. Kato, *Applied Physics Letters* **112**, 021101 (2018).

[14] T. Ando, *J. Phys. Soc. Jpn.* **74**, 777 (2005).

[15] M. J. O'Connell, S. M. Bachilo, C. B. Huffman, V. C. Moore, M. S. Strano, E. H. Haroz, K. L. Rialon, P. J. Boul, W. H. Noon, C. Kittrell, J. Ma, R. H. Hauge, R. B. Weisman, R. E. Smalley, *Science* **297**, 593 (2002).

[16] S. M. Bachilo, M. S. Strano, C. Kittrell, R. H. Hauge, R. E. Smalley, R. B. Weisman, *Science* **298**, 2361 (2002).

[17] R. B. Weisman, S. M. Bachilo, *Nano Lett.* **3**, 1235 (2003).

[18] Y. Ohno, S. Iwasaki, Y. Murakami, S. Kishimoto, S. Maruyama, T. Mizutani, *Phys. Rev. B* **73**, 235427 (2006).

[19] T. Mueller, M. Kinoshita, M. Steiner, V. Perebeinos, A. A. Bol, D. B. Farmer, P. Avouris, *Nat. Nanotech.* **5**, 27 (2010).

[20] H. Zhao, S. Mazumdar, *Phys. Rev. Lett.* **93**, 157402 (2004).

[21] S. Uryu, T. Ando, *Phys. Rev. B* **74**, 155411 (2006).

[22] T. Ogawa, T. Takagahara, *Phys. Rev. B* **44**, 8138 (1991).

[23] F. Wang, G. Dukovic, L. E. Brus, T. F. Heinz, *Science* **308**, 838 (2005).

[24] J. Maultzsch, R. Pomraenke, S. Reich, E. Chang, D. Prezzi, A. Ruini, E. Molinari, M. S. Strano, C. Thomsen, C. Lienau, *Phys. Rev. B* **72**, 241402(R) (2005).

[25] J. Lefebvre, P. Finnie, *Nano Lett.* **8**, 1890 (2008).

[26] Y. Kimoto, M. Okano, Y. Kanemitsu, *Phys. Rev. B* **87**, 195416 (2013).

[27] J. Lefebvre, P. Finnie, *Phys. Rev. Lett.* **98**, 167406 (2007).

[28] T. Ando, *J. Phys. Soc. Jpn.* **75**, 024707 (2006).

[29] E. B. Barros, R. B. Capaz, A. Jorio, G. G. Samsonidze, A. G. Souza Filho, S. Ismail-Beigi, C. D. Spataru, S. G. Louie, G. Dresselhaus, M. S. Dresselhaus, *Phys. Rev. B* **73**, 241406 (2006).

[30] I. B. Mortimer, R. J. Nicholas, *Phys. Rev. Lett.* **98**, 027404 (2007).

[31] R. Matsunaga, Y. Miyauchi, K. Matsuda, Y. Kanemitsu, *Phys. Rev. B* **80**, 115436 (2009).

[32] S. Zaric, G. N. Ostojic, J. Kono, J. Shaver, V. C. Moore, M. S. Strano, R. H. Hauge, R. E. Smalley, X. Wei, *Science* **304**, 1129 (2004).

[33] J. Shaver, J. Kono, O. Portugall, V. Krstic, G. L. J. A. Rikken, Y. Miyauchi, S. Maruyama, V. Perebeinos, *Nano Lett.* **7**, 1851 (2007).

[34] R. Matsunaga, K. Matsuda, Y. Kanemitsu, *Phys. Rev. Lett.* **101**, 147404 (2008).

[35] K. Matsuda, T. Inoue, Y. Murakami, S. Maruyama, Y. Kanemitsu, *Phys. Rev. B* **77**, 193405 (2008).

[36] H. Harutyunyan, T. Gokus, A. A. Green, M. C. Hersam, M. Allegrini, A. Hartschuh, *Nano Lett.* **9**, 2010 (2009).

[37] K. Matsuda, Y. Miyauchi, T. Sakashita, Y. Kanemitsu, *Phys. Rev. B* **81**, 033409 (2010).

[38] A. D. Mohite, T. S. Santos, J. S. Moodera, B. W. Alphenaar, *Nat. Photon.* **4**, 425 (2009).

[39] K. Nagatsu, S. Chiashi, S. Konabe, Y. Homma, *Phys. Rev. Lett.* **105**, 157403 (2010).

[40] D. Stich, F. Späth, H. Kraus, A. Sperlich, V. Dyakonov, T. Hertel, *Nat. Photon.* **8**, 139 (2014).

[41] C. Fantini, A. Jorio, M. Souza, M. S. Strano, M. S. Dresselhaus, M. A. Pimenta, *Phys. Rev. Lett.* **93**, 147406 (2004).

[42] D. A. Heller, E. S. Jeng, T.-K. Yeung, B. M. Martinez, A. E. Moll, J. B. Gastala, M. S. Strano, *Science* **311**, 508 (2006).

[43] J. Lefebvre, J. M. Fraser, Y. Homma, P. Finnie, *Appl. Phys. A* **78**, 1107 (2004).

[44] Z. Wang, H. Pedrosa, T. Krauss, L. Rothberg, *Phys. Rev. Lett.* **96**, 047403 (2006).

[45] Y.-Z. Ma, L. Valkunas, S. M. Bachilo, G. R. Fleming, *The Journal of Physical Chemistry B* **109**, 15671 (2005).

[46] P. Finnie, Y. Homma, J. Lefebvre, *Phys. Rev. Lett.* **94**, 247401 (2005).

[47] D. E. Milkie, C. Staii, S. Paulson, E. Hindman, A. T. Johnson, J. M. Kikkawa, *Nano Lett.* **5**, 1135 (2005).

[48] S. Moritsubo, T. Murai, T. Shimada, Y. Murakami, S. Chiashi, S. Maruyama, Y. K. Kato, *Phys. Rev. Lett.* **104**, 247402 (2010).

[49] Y. Homma, S. Chiashi, T. Yamamoto, K. Kono, D. Matsumoto, J. Shitaba, S. Sato, *Phys. Rev. Lett.* **110**, 157402 (2013).

[50] A. Akaishi, T. Yonemaru, J. Nakamura, *ACS Omega* **2**, 2184 (2017).

[51] T. Uda, M. Yoshida, A. Ishii, Y. K. Kato, *Nano Lett.* **16**, 2278 (2016).

[52] A. Ishii, M. Yoshida, Y. K. Kato, *Phys. Rev. B* **91**, 125427 (2015).

[53] H. Zhao, S. Mazumdar, *Phys. Rev. Lett.* **98**, 166805 (2007).

[54] Y. Kumamoto, M. Yoshida, A. Ishii, A. Yokoyama, T. Shimada, Y. K. Kato, *Phys. Rev. Lett.* **112**, 117401 (2014).

[55] M. Barkelid, V. Zwiller, *Nat. Photon.* **8**, 47 (2014).

[56] S. Kazaoui, S. Cook, N. Izard, Y. Murakami, S. Maruyama, N. Minami, *J. Phys. Chem. C* **118**, 18059 (2014).

[57] J. Park, O. G. Reid, J. L. Blackburn, G. Rumbles, *Nat. Commun.* **6**, 8809 (2015).

[58] A. D. Mohite, P. Gopinath, H. M. Shah, B. W. Alphenaar, *Nano Lett.* **8**, 142 (2008).

[59] M. Yoshida, Y. Kumamoto, A. Ishii, A. Yokoyama, Y. K. Kato, *Appl. Phys. Lett.* **105**, 161104 (2014).

[60] V. Perebeinos, P. Avouris, *Nano Lett.* **7**, 609 (2007).

[61] M. H. Ham, B. S. Kong, W. J. Kim, H. T. Jung, M. S. Strano, *Phys. Rev. Lett.* **102**, 047402 (2009).

[62] H. Kishida, Y. Nagasawa, S. Imamura, A. Nakamura, *Phys. Rev. Lett.* **100**, 097401 (2008).

[63] T. Ando, *J. Phys. Soc. Jpn.* **78**, 104703 (2009).

[64] G. Dukovic, F. Wang, D. Song, M. Y. Sfeir, T. F. Heinz, L. E. Brus, *Nano Lett.* **5**, 2314 (2005).

[65] V. Perebeinos, J. Tersoff, P. Avouris, *Phys. Rev. Lett.* **92**, 257402 (2004).

[66] H. A. Bethe, E. E. Salpeter, *Quantum Mechanics of One- and Two- Electron Atoms* (Academic, New York, 1957).

[67] H. J. Caulfield, S. Dolev, *Nat. Photon.* **4**, 261 (2010).

[68] M. Khajavikhan, A. Simic, M. Katz, J. H. Lee, B. Slutsky, A. Mizrahi, V. Lomakin, Y. Fainman, *Nature* **482**, 204 (2012).

[69] M. Hochberg, T. Baehr-Jones, G. Wang, M. Shearn, K. Harvard, J. Luo, B. Chen, Z. Shi, R. Lawson, P. Sullivan, A. K. Y. Jen, L. Dalton, A. Scherer, *Nat. Mater.* **5**, 703 (2006).

[70] H. Gibbs, *Optical Bistability: Controlling Light with Light* (Academic Press, Orlando, 1985).

[71] V. R. Almeida, M. Lipson, *Opt. Lett.* **29**, 2387 (2004).

[72] M. T. Hill, H. J. S. Dorren, T. de Vries, X. J. M. Leijtens, J. H. den Besten, B. Smalbrugge, Y.-S. Oei, H. Binsma, G.-D. Khoe, M. K. Smit, *Nature* **432**, 206 (2004).

[73] T. Mori, Y. Yamayoshi, H. Kawaguchi, *Appl. Phys. Lett.* **88**, 101102 (2006).

[74] L. Liu, R. Kumar, K. Huybrechts, T. Spuesens, G. Roelkens, E.-J. Geluk, T. de Vries, P. Regreny, D. Van Thourhout, R. Baets, G. Morthier, *Nat. Photon.* **4**, 182 (2010).

[75] K. Nozaki, A. Shinya, S. Matsuo, Y. Suzaki, T. Segawa, T. Sato, Y. Kawaguchi, R. Takahashi, M. Notomi, *Nat. Photon.* **6**, 248 (2012).

[76] E. Kuramochi, K. Nozaki, A. Shinya, K. Takeda, T. Sato, S. Matsuo, H. Taniyama, H. Sumikura, M. Notomi, *Nat. Photon.* **8**, 474 (2014).

[77] E. Gaufrès, N. Izard, A. Noury, X. Le Roux, G. Rasigade, A. Beck, L. Vivien, *ACS Nano* **6**, 3813 (2012).

[78] A. Högele, C. Galland, M. Winger, A. Imamoğlu, *Phys. Rev. Lett.* **100**, 217401 (2008).

[79] A. Ishii, T. Uda, Y. K. Kato, *Phys. Rev. Applied* **8**, 054039 (2017).

[80] H. Ajiki, T. Ando, *Physica B: Condensed Matter* **201**, 349 (1994).

[81] K. Liu, X. Hong, Q. Zhou, C. Jin, J. Li, W. Zhou, J. Liu, E. Wang, A. Zettl, F. Wang, *Nat. Nanotech.* **8**, 917 (2013).

[82] Y. Miyauchi, R. Saito, K. Sato, Y. Ohno, S. Iwasaki, T. Mizutani, J. Jiang, S. Maruyama, *Chem. Phys. Lett.* **442**, 394 (2007).

[83] Y.-F. Xiao, M. D. Anderson, J. M. Fraser, *Phys. Rev. B* **89**, 235440 (2014).

[84] T. Uda, A. Ishii, Y. K. Kato, *ACS Photonics* (published online 2017). DOI: 10.1021/acsphotonics.7b01104.

[85] C. Georgi, N. Hartmann, T. Gokus, A. A. Green, M. C. Hersam, A. Hartschuh, *Chem. Phys. Chem.* **9**, 1460 (2008).

[86] K. Yoshikawa, K. Matsuda, Y. Kanemitsu, *J. Phys. Chem. C* **114**, 4353 (2010).

[87] J. Lefebvre, P. Finnie, Y. Homma, *Phys. Rev. B* **70**, 045419 (2004).

[88] K. Matsuda, T. Inoue, Y. Murakami, S. Maruyama, Y. Kanemitsu, *Phys. Rev. B* **77**, 033406 (2008).

[89] K. Yoshikawa, R. Matsunaga, K. Matsuda, Y. Kanemitsu, *Appl. Phys. Lett.* **94**, (2009).

[90] A. W. Adamson, *Physical chemistry of surfaces* (Wiley, New York, 1990).

[91] S. Berber, Y.-K. Kwon, D. Tománek, *Phys. Rev. Lett.* **84**, 4613 (2000).

[92] M. Fujii, X. Zhang, H. Xie, H. Ago, K. Takahashi, T. Ikuta, H. Abe, T. Shimizu, *Phys. Rev. Lett.* **95**, 065502 (2005).

[93] C. Yu, L. Shi, Z. Yao, D. Li, A. Majumdar, *Nano Lett.* **5**, 1842 (2005).

List of publications and presentations

Publications

[1] H. Machiya, T. Uda, A. Ishii, and Y. K. Kato, "Spectral tuning of optical coupling between air-mode nanobeam cavities and individual carbon nanotubes", *Appl. Phys. Lett.* **112,** 021101 (2018).

[2] T. Uda, A. Ishii, and Y. K. Kato, "Single carbon nanotubes as ultrasmall all-optical memories", *ACS Photonics* (published online 2017), DOI: 10.1021/acsphotonics.7b01104.

[3] A. Ishii, T. Uda, and Y. K. Kato, "Room-Temperature Single-Photon Emission from Micrometer-Long Air-Suspended Carbon Nanotubes", *Phys. Rev. Applied* **8,** 054039 (2017).

[4] N. Higashide, M. Yoshida, T. Uda, A. Ishii, and Y. K. Kato, "Cold exciton electroluminescence from air-suspended carbon nanotube split-gate devices", *Appl. Phys. Lett.* **110,** 191101 (2017).

[5] T. Uda, M. Yoshida, A. Ishii, and Y. K. Kato, "Electric-Field Induced Activation of Dark Excitonic States in Carbon nanotubes", *Nano Lett.* **16,** 2278 (2016).

Oral presentations (International conferences)

[6] T. Uda, A. Ishii, Y. K. Kato, "Single carbon nanotubes as ultrasmall all-optical memories", March Meeting of the American Physical Society, Los

Angeles, California, USA (March 6, 2018).

[7] T. Uda, M. Yoshida, A. Ishii, Y. K. Kato, "Electrical Activation of Dark Excitonic States in Carbon Nanotubes", March Meeting of the American Physical Society, Baltimore, Maryland, USA (March 15, 2016).

[8] T. Uda, Y. Kumamoto, M. Yoshida, A. Ishii, Y. K. Kato, "Photoconductivity spectroscopy of individual suspended carbon nanotubes", 8th International Workshop on Metrology, Standardization and Industrial Quality of Nanotubes (MSIN14), Los Angeles, California, USA (June 1, 2014).

Poster presentations (International conferences)

[9] T. Uda, M. Yoshida, A. Ishii, Y. K. Kato, "Electrical activation of dark excitonic states in carbon nanotubes", Fundamental optical processes in semiconductors (FOPS), Breckenridge, Colorado, USA (August 6, 2015).

[10] T. Uda, M. Yoshida, A. Ishii, Y. K. Kato, "Electrical activation of dark excitonic states in carbon nanotubes", The Sixteenth International Conference on the Science and Application of Nanotubes (NT15), Nagoya, Japan (June 30, 2015).

[11] T. Uda, M. Yoshida, A. Ishii, Y. K. Kato, "Electrical activation of dark excitonic states in carbon nanotubes", Ninth International Workshop on Metrology, Standardization and Industrial Quality of Nanotubes (MSIN15), Nagoya, Japan (June 28, 2015).

[12] T. Uda, M. Yoshida, A. Ishii, Y. K. Kato, "Electrical activation of dark excitonic states in carbon nanotubes", 6th Workshop on Nanotube Optics and Nanospectroscopy (WONTON15), Kloster Banz, Germany (June 3, 2015).

[13] T. Uda, Y. Kumamoto, M. Yoshida, A. Ishii, Y. K. Kato, "Photoconductivity spectroscopy of individual suspended carbon nanotubes", The Fif-

teenth International Conference on the Science and Application of Nanotubes (NT14), Los Angeles, California, USA (June 2, 2014).

Oral presentations (Domestic conferences)

[14] T. Uda, A. Ishii, Y. K. Kato, "Optical bistability in carbon nanotubes", The 64th March Meeting of the Japan Society of Applied Physics, Kanagawa (March 15, 2017).

[15] T. Uda, A. Ishii, Y. K. Kato, "Optical bistability in carbon nanotubes", The 52nd Fullerenes-Nanotubes-Graphene General Symposium, Tokyo (March 3, 2017).

[16] T. Uda, M. Yoshida, A. Ishii, Y. K. Kato, "Electrical activation of dark excitonic states in carbon nanotubes", The 49th Fullerenes-Nanotubes-Graphene General Symposium, Kita-Kyushu (September 9, 2015).

Poster presentations (Domestic conferences)

[17] T. Uda, M. Yoshida, A. Ishii, Y. K. Kato, "Bias-voltage induced absorption peaks in individual suspended carbon nanotubes", The 48th Fullerenes-Nanotubes-Graphene General Symposium, Tokyo (February 21, 2015).

[18] T. Uda, Y. Kumamoto, M. Yoshida, A. Ishii, Y. K. Kato, "Photoconductivity spectroscopy of individual suspended carbon nanotubes", The 46th Fullerenes-Nanotubes-Graphene General Symposium, Tokyo (March 5, 2014).